STUDY OF DENSITY LIMIT IN JT-60 JOULE HEATED PLASMAS

November 1995

Hiroshi SHIRAI, Katsuhiro SHIMIZU, Tomonori TAKIZUKA
Toshio HIRAYAMA and Masafumi AZUMI

日 本 原 子 力 研 究 所
Japan Atomic Energy Research Institute

Study of Density Limit in JT-60 Joule Heated Plasmas

Hiroshi SHIRAI, Katsuhiro SHIMIZU, Tomonori TAKIZUKA
Toshio HIRAYAMA and Masafumi AZUMI

Department of Fusion Plasma Research
Naka Fusion Research Establishment
Japan Atomic Energy Research Institute
Naka-machi, Naka-gun, Ibaraki-ken

Impurities which mingle in tokamak plasmas cause dominant radiation loss in the high density regime and the energy balance of plasma is lost. This gives rise to MHD instability and results in major disruption. Density limit in joule heated plasmas has been studied by using one dimensional transport code combined with MHD instability analysis code. When the diffusion of impurity is taken into account, the numerically obtained density limit diagram or Hugill diagram quantitatively agrees well with that obtained in the experiment. It is also clarified that the corona-equilibrium model overestimates the density limit.

ＪＴ－６０ジュール加熱プラズマにおける密度限界の研究

日本原子力研究所那珂研究所炉心プラズマ研究部

白井　　浩・清水　勝宏・滝塚　知典

平山　俊雄・安積　正史

トカマクプラズマに混入した不純物は，高密度領域における大きい放射損失によりプラズマのエネルギーバランスを崩し，ＭＨＤ不安定性を誘発してディスラプションを引き起こす。一次元輸送コードにＭＨＤ不安定性解析コードを結合し，ジュール加熱プラズマにおける密度限界の研究を行った。不純物の拡散過程を考慮したモデルを用いた数値計算では，密度限界ダイアグラムすなわちHugillダイアグラムは，実験で得られたものと定量的に良く一致した。また，コロナ平衡モデルは密度限界値を過大に評価することを示した。

那珂研究所：〒311-01　茨城県那珂郡那珂町向山　801-1

Contents

目　　　　次

1. Introduction

Various kinds of operational limit exist in the tokamak discharges. Density limit is one of the important ones to be studied in detail for the development of ITER (International Thermonuclear Engineering Reactor), because high density operation is planned in ITER in order to achieve high Q value.[1]

In high density discharges of tokamaks, especially with large impurity content, are often terminated by the major disruption.[2] This operational limit is described in the diagram showing the plasma current versus density or Murakami parameter $\bar{n}_e R/B_t$,[3] where B_t is a toroidal magnetic field and R is a major radius. This diagram is so-called the Hugill diagram.[4]

In the high density plasma, the radiation loss or excitation loss by impurity ions affects the total energy balance significantly. When the total radiation loss becomes comparable to the input power, the plasma current channel begins to shrink since the plasma temperature cannot be sustained by the outward heat flux from the central region. When the gradient of plasma current density at the resonant surface become large, tearing modes with low poloidal mode number become strongly destabilized.[5] In this paper, the above whole processes are studied numerically by using one dimensional transport code combined with MHD instability analysis code.

Various kinds of the impurity species are observed in tokamaks. In case of light impurities such as carbon and oxygen, the radiation loss concentrates in the plasma peripheral region, since they are fully ionized in the central region. In case of heavy impurities or metal impurities such as titanium and molybdenum, the radiation loss easily expands into the plasma central region. In this paper, we compare both cases and clarify difference towards the major disruptions due to the impurity species.

In Section 2, the numerical model to simulate high density plasmas in JT-60 tokamak are explained. In Section 3, numerical results for high density plasmas without impurities are presented in order to compare with results for impurity-contaminated plasmas to evaluate the impurity effects on the density limit. Numerical results for high density plasmas with light impurity species and those with metal impurity species are presented in Sections 4 and 5, respectively. Comparison of the Hugill diagram between numerical results and experimental data is shown for ohmically heated plasmas of JT-60 in Section 6 . Results obtained in this paper are summarized in Section 7 .

2. Numerical Calculation Method

2.1. Bulk Plasma Transport

In this paper numerical calculations are carried out by using the one dimensional (1-D) tokamak transport code[6] combined with MHD stability code. The latter one will be explained in Sections 2.4 and 2.5 . Equations describing bulk tokamak transport are expressed as follows;

$$\frac{\partial n_i}{\partial t} = -\frac{1}{r}\frac{\partial}{\partial r}(r\Gamma_i) + S \; , \tag{1}$$

$$\frac{3}{2}\frac{\partial}{\partial t}(n_e T_e) = -\frac{1}{r}\frac{\partial}{\partial r}(rQ_e) + Q_{OH} - Q_{eq}^{e\rightarrow i} - Q_{rad} + Q_n^e \; , \tag{2}$$

$$\frac{3}{2}\frac{\partial}{\partial t}(n_i T_i) = -\frac{1}{r}\frac{\partial}{\partial r}(rQ_i) + Q_{eq}^{e\rightarrow i} - Q_{cx} + Q_n^i \; , \tag{3}$$

$$\frac{\partial B_p}{\partial t} = \frac{\partial}{\partial r}\left\{\frac{\eta}{r}\frac{\partial}{\partial r}(rB_p)\right\} \; . \tag{4}$$

Time evolution of ion density, n_i, electron temperature, T_e, ion temperature, T_i, and poloidal magnetic field, B_p, are governed by these equations. Here, Q_{OH} is ohmic heating power equal to ηJ_z^2, where J_z is a toroidal plasma current density and η is a neoclassical resistivity.[7] Γ_i is an ion particle flux, Q_e and Q_i are an electron and an ion heat flux, respectively. Both ionization and recombination processes are considered in the particle source, S.

The ion particle and electron flux, Γ_i and Γ_e, are written as

$$\Gamma_i = \Gamma_e = -D\frac{\partial n_i}{\partial r} - n_i V_{Ware} \; , \tag{5}$$

where D is the particle diffusion coefficient and V_{Ware} is the inward particle flow velocity by Ware pinch.[8] The electron and ion heat fluxes are written as follows;

$$Q_e = -n_e \chi_e \frac{\partial T_e}{\partial r} + \frac{3}{2}T_e \Gamma_e \; , \tag{6}$$

$$Q_i = -n_i \chi_i \frac{\partial T_i}{\partial r} + \frac{3}{2}T_i \Gamma_i \; , \tag{7}$$

Here χ_e and χ_i are the electron and ion thermal diffusivity, respectively. In this paper transport coefficients are set as follows,

$$D = \frac{1 \times 10^{19}}{n_e} \; , \tag{8}$$

$$\chi_e = 10^{21}\frac{r}{n_e q R^2} \; , \tag{9}$$

$$\chi_i = 1.5\chi_i^{NC} \; . \tag{10}$$

In the above formula, χ_e is consistent with neo-Alcator scaling.

The energy flow from electrons to ions is denoted as $Q_{eq}^{\,e\rightarrow i}$. The radiation loss, Q_{rad}, is made up of several atomic processes such as Bremsstrahlung, cyclotron radiation, excitation loss and so forth. Q_{cx} is the charge exchange loss. Q_n^e and Q_n^i are the energy gain and loss related to both ionization and recombination.

Hydrogen neutrals injected by gas puffing or released from the first wall by recycling. The energy of these neutrals are set 5 eV, which is the same as boundary temperature.

2.2. Impurity Transport

The time evolution of impurity density in the charge state k (k=1,2,$\cdots$,Z_A), n_k, is described as follows;

$$\frac{\partial n_k}{\partial t} = -\frac{1}{r}\frac{\partial}{\partial r}\left(r\Gamma_k\right) + S_k \ , \tag{11}$$

where the impurity flux is

$$\Gamma_k = -D_Z\frac{\partial n_k}{\partial r} - V_A n_k \tag{12}$$

and

$$D_Z = D_Z^{NC} + D_A \ . \tag{13}$$

D_Z^{NC} is the diffusion coefficient of impurity derived from the neoclassical theory.[9,10] D_A is the anomalous diffusion coefficient of impurity. Since the magnitude of D_Z^{NC} is very small for the JT-60 plasma parameters, it is negligible in eq.(13). V_A is the anomalous inward flow velocity of impurity. It is assumed as follows,[11]

$$V_A = D_A C_A\frac{2r}{a^2} \ , \tag{14}$$

where the coefficient C_A is related to the impurity density profile. In this paper, D_A=1.0 m^{2}sec^{-1} and C_A=1 are assumed to reproduce impurity density profile in JT-60 plasmas reasonably.

The impurity source term is described as

$$\begin{aligned} S_k &= n_e\left(n_{k-1}\alpha_{k-1} - n_k\alpha_k + n_{k+1}\beta_{k+1} - n_k\beta_k\right)\\ &+ n_{z0}\left(n_{k+1}\beta_{k+1}^{CT} - n_k\beta_k^{CT}\right) \ , \end{aligned} \tag{15}$$

where α_k is the ionization rate from charge state k to $k+1$, β_k is the recombination rate from charge state k to $k-1$, respectively, n_{z0} is the neutral

impurity density and β_k^{CT} is the charge transfer recombination rate.[12] Here neutral impurity is assumed to be puffed from the first wall with the temperature T_{z0}=5 eV. The amount of impurity puff is decided in order to keep the given impurity content.

The temperature of impurity, T_k, is assumed to be the same as bulk hydrogen species because the energy relaxation time between hydrogen and impurity is much shorter than the energy confinement time, τ_E.

The radiative cooling rate, L_Z, and the average charge state, $\langle Z \rangle$, as a function of electron temperature for carbon, oxygen, titanium and molybdenum are shown in Fig. 1.[13] The average ion model[14] is adopted in this figure. The radiation can be estimated by

$$Q_{rad} = L_Z \, n_e \sum_{k=1}^{Z_A} n_k \ . \tag{16}$$

The average charge state is defined as

$$\langle Z \rangle = \frac{\displaystyle\sum_{k=1}^{Z_A} k \, n_k}{\displaystyle\sum_{k=1}^{Z_A} n_k} \ . \tag{17}$$

From Fig. 1, it is found that carbon and oxygen easily become fully ionized impurity ions in JT-60 ohmically heated plasmas with $T_e(0)$=1~3 keV.

2.3. Scrape-off Plasma Transport

The transport properties of scrape-off plasma affects the bulk plasma significantly by changing the boundary density and temperature. In this paper, the scrape-off layer with the thickness of 4 cm is set up outside the surface of the bulk plasma. In this layer, loss rates of particles, electron energy and ion energy along the magnetic field line are expressed as $n_i/\tau_{\parallel}$, $3\gamma_e n_e T_e/2\tau_{\parallel}$ and $3\gamma_i n_i T_i/2\tau_{\parallel}$, respectively. Here the heat transmission coefficients are set as γ_e=5.8 and γ_i=2.0 according to the sheath theory.[15] The life time of particle along the magnetic field line, $\tau_{\parallel}$=L/V_f, is estimated by using the connection length, L=$\pi q R$, and the flow velocity V_f. The flow velocity is assumed V_f=$C_S/3$, where C_S=$\sqrt{T_e/m_i}$ is the ion sound velocity in the scrape-off layer.

The cross-field transport coefficients in this layer are assumed spatially constant and Bohm type[16-18];

$$D = \chi_e = \chi_i = C_B \frac{T_e^{SEP}}{16eB} \ , \tag{18}$$

where T_e^{SEP} is the electron temperature at the separatrix. The coefficient C_B is set 0.5 . The electron and ion temperatures are fixed at 5 eV for the outer boundary of the scrape-off layer. These values are not sensitive for transport code results. The value of T_e^{SEP} is determined by both the energy flux into the separatrix from the bulk plasma and the energy loss rate in the scrape-off plasma. Similarly, n_e^{SEP} and T_i^{SEP} are also calculated. It is reasonable to assume no plasma current in the scrape-off layer. Thus the boundary condition of plasma current at the separatrix is $J_z^{SEP}=0$.

2.4. Modeling of Sawtooth Oscillation

When the safety factor, q, at the plasma center falls below unity, the tearing mode with poloidal mode number $m=1$ and toroidal mode number $n=1$ becomes unstable. Then the magnetic island is formed around $q=1$ resonant surface at $r=r_s$ due to the magnetic field line reconnection. The time evolution of magnetic island width, W, is calculated as follows,

$$W = W_0 \exp\left(\int_0^t \gamma(t')dt'/2\right) \ , \tag{19}$$

where W_0 is the small initial island width. In this paper $W_0=10^{-4}$ m is assumed. γ is the growth rate of the tearing mode including the diamagnetic effect.[19]

When W becomes greater than r_s, the initial hot core plasma in the central region moves to the peripheral region. This phenomena is called the internal disruption. At the internal disruption, the magnetic flux exchange occurs. At the same time, the safety factor becomes larger than one again.

The way of magnetic flux exchange is proposed by Kadomtsev.[20] First the helical flux function ψ is defined as

$$\psi(r) = \frac{B_t}{R} \int_0^r \left(\frac{1}{q} - 1\right) r dr \tag{20}$$

in the cylindrical plasma. The critical radius, r_c, is determined by $\psi(r_c)=0$. In the region $0 \leq r \leq r_c$, the magnetic flux exchange occurs.

Before and after the internal disruption, the following relation holds from the helical flux conservation;

$$r_1 dr_1 + r_2 dr_2 = r dr \ , \tag{21}$$

$$\psi^B(r_1) = \psi^B(r_2) = \psi^A(r) \ , \tag{22}$$

$$\psi^B(r_1 + dr_1) = \psi^B(r_2 - dr_2) = \psi^A(r - dr) \ . \tag{23}$$

Superscripts "B" and "A" are adopted to distinguish the plasma parameters "before" and "after" the minor disruption. By applying Taylor expansion to eq.(23),

$$\frac{1}{r}\frac{d\psi^A}{dr} = -\frac{\psi_1'\psi_2'}{r_1\psi_2' - r_2\psi_1'} \tag{24}$$

is obtained from eq.(21), where

$$\psi_1' = \left.\frac{d\psi^B}{dr}\right|_{r_1} \ , \qquad \psi_2' = \left.\frac{d\psi^B}{dr}\right|_{r_2} \ .$$

The safety factor after the internal disruption is calculated from eq.(24) as

$$q^A = \frac{1}{\dfrac{R}{B_t}\dfrac{d\psi^A}{dr} + 1} \ . \tag{25}$$

Thus the poloidal magnetic field, B_p or the toroidal plasma current, J_z, after the internal disruption is obtained from eq.(25).

It is assumed that density and pressure profiles in $0 \le r \le r_c$ becomes entirely flat at the internal disruption, that is,

$$\int_0^{r_c} n_e^B(r)r dr = n_e^A \int_0^{r_c} r dr \ , \tag{26}$$

$$\int_0^{r_c} n_i^B(r)r dr = n_i^A \int_0^{r_c} r dr \ , \tag{27}$$

$$\int_0^{r_c} n_e^B(r)T_e^B(r)r dr = n_e^A T_e^A \int_0^{r_c} r dr \ , \tag{28}$$

$$\int_0^{r_c} n_i^B(r)T_i^B(r)r dr = n_i^A T_i^A \int_0^{r_c} r dr \ . \tag{29}$$

In this model density and pressure are conserved at the internal disruption.

2.5. Magnetic Island Formation due to Tearing Mode

When the tearing mode is unstable at $q = m/n$ (>1) resonant surface, the magnetic island is formed due to the magnetic field reconnection. The stability condition of tearing mode is determined by the following relation,

$$\Delta'(0) = \lim_{\varepsilon \to 0}\left\{\left.\frac{d\Psi}{dr}\right|_{r_s+\varepsilon} - \left.\frac{d\Psi}{dr}\right|_{r_s-\varepsilon}\right\} / \Psi(r_s) \ , \tag{30}$$

where Ψ is a perturbed helical flux function, which is connected with the radial perturbed magnetic field, $\widetilde{B_r} = i \ \Psi(r) \exp(\gamma t + im\theta + in\varphi)$. When $\Delta'(0) > 0$,

plasma is unstable against the tearing mode.[5] In such a case, the magnetic island is formed due to the magnetic field reconnection at $r=r_s$.

After the linear growth phase, the tearing mode proceeds to a saturated phase with a finite width of magnetic island. The saturated island width W is estimated by the following formula,[21,22]

$$\frac{dW}{dt} = 1.66\frac{\eta(r_s)}{\mu_0}\Delta'(W) \ ,\tag{31}$$

where

$$\Delta'(W) = \left\{ \frac{d(r\Psi)}{dr}\bigg|_{r_s+W/2} - \frac{d(r\Psi)}{dr}\bigg|_{r_s-W/2} \right\} / (r_s\Psi(r_s)) \ .\tag{32}$$

Since the magnetic field line is connected across the magnetic island, the particle and energy transport are significantly enhanced in this region. In this paper, χ_e is enhanced by a factor of 100 in the region $r_s - W/2 < r < r_s + W/2$.

2.6. Procedure of Numerical Simulation

The transport analyses are carried out for the following JT-60 plasma parameters: $R=3.03$ m, $a=0.95$ m, $B_t=4.5$ T, $I_p=1\sim2.3$ MA. The radius of separatrix is 0.92 m. For the numerical simulation 48 mesh points in the main plasma are adopted and 6 mesh points are adopted in the scrape-off plasma.

In the simulation carbon, oxygen, titanium and molybdenum are selected as the impurity species. The impurity content, I_{imp}, is given by the ratio of the number of total impurities to the number of total hydrogen ion as

$$I_{imp} = \frac{\displaystyle\int_V \sum_{k=1}^{Z_A} n_k dV}{\displaystyle\int_V n_i dV} \ .\tag{33}$$

In this paper I_{imp} is assumed 6 % for carbon, 0.5, 1, 2 and 4 % for oxygen, 0.05 % for titanium, and 0.01 % for molybdenum. I_{imp} is set constant during the time evolution.

In the simulation, the initial profiles of n_i, T_e, T_i and J_z are given. Then these profiles are calculated for one second by using the transport code in order to obtain the steady state. During this period, the total ion density is kept constant. Then hydrogen puff is started with constant rate. Since I_{imp} is set constant, the total number of impurities in the plasma also increases with the plasma density.

The gas puffing rates are set as 2×10^{19} m^{-3}sec^{-1} for the case without impurity, 5×10^{18} m^{-3}sec^{-1} for the light impurity cases and 2×10^{18} m^{-3}sec^{-1} for the metal impurity cases. This gas puffing rate is set as low as possible within a limitation of computational time in order to avoid the sudden plasma edge cooling.

Sawtooth oscillation and the magnetic island formation by destabilized (2,1) and (3,2) tearing mode are simulated all through the numerical calculation. When one of the following conditions (a)~(c) is satisfied, it is considered that the major disruption occurs.

(a)   (2,1) island and (3,2) island are overlapped.[23]

(b)   (2,1) island grows and contacts the sawtooth region.

(c)   (2,1) island grows and contacts the first wall.

The numerical simulation is executed until one of the conditions (a)~(c) is satisfied. Thus the maximum attainable electron density for the fixed impurity content I_{imp} is obtained by the numerical simulation. By changing the plasma parameters such as plasma current, impurity species, impurity content and so forth, the operation limit about the maximum density is drawn on the Hugill diagram.

In the numerical simulation, the density profiles of impurity in each charge state is calculated by eq.(11). It is called the impurity diffusion model. The corona-equilibrium model is also used to determine the ratio of impurity density in each charge state.[24] Since the corona-equilibrium model does not determine the spatial impurity density profile by itself, the assumption

$$\sum_k n_k \propto e^{-C_A\left(\frac{r}{a}\right)^2} \ . \tag{34}$$

is adopted. The numerical results by the corona-equilibrium model are compared with those obtained by the impurity diffusion model. Thus the validity of the corona-equilibrium model is examined for the JT-60 plasma parameters.

3.   Density Limit of Plasmas without Impurity

By executing a long time discharge cleaning to tokamak plasmas after the baking of the first wall, impurity content decreases significantly. However, they cannot be removed completely. The impurity free plasma is unrealistic in the experiment. In this Section, however, the high density impurity free plasma will be studied in order to highlight the effect of radiation cooling by

The gas puffing rates are set as 2×10^{19} m^{-3}sec^{-1} for the case without impurity, 5×10^{18} m^{-3}sec^{-1} for the light impurity cases and 2×10^{18} m^{-3}sec^{-1} for the metal impurity cases. This gas puffing rate is set as low as possible within a limitation of computational time in order to avoid the sudden plasma edge cooling.

Sawtooth oscillation and the magnetic island formation by destabilized (2,1) and (3,2) tearing mode are simulated all through the numerical calculation. When one of the following conditions (a)∼(c) is satisfied, it is considered that the major disruption occurs.

(a)   (2,1) island and (3,2) island are overlapped.[23]

(b)   (2,1) island grows and contacts the sawtooth region.

(c)   (2,1) island grows and contacts the first wall.

The numerical simulation is executed until one of the conditions (a)∼(c) is satisfied. Thus the maximum attainable electron density for the fixed impurity content I_{imp} is obtained by the numerical simulation. By changing the plasma parameters such as plasma current, impurity species, impurity content and so forth, the operation limit about the maximum density is drawn on the Hugill diagram.

In the numerical simulation, the density profiles of impurity in each charge state is calculated by eq.(11). It is called the impurity diffusion model. The corona-equilibrium model is also used to determine the ratio of impurity density in each charge state.[24] Since the corona-equilibrium model does not determine the spatial impurity density profile by itself, the assumption

$$\sum_k n_k \propto e^{-C_A \left(\frac{r}{a} \right)^2} \ . \tag{34}$$

is adopted. The numerical results by the corona-equilibrium model are compared with those obtained by the impurity diffusion model. Thus the validity of the corona-equilibrium model is examined for the JT-60 plasma parameters.

3.   Density Limit of Plasmas without Impurity

By executing a long time discharge cleaning to tokamak plasmas after the baking of the first wall, impurity content decreases significantly. However, they cannot be removed completely. The impurity free plasma is unrealistic in the experiment. In this Section, however, the high density impurity free plasma will be studied in order to highlight the effect of radiation cooling by

light impurities or metal impurities, which will be discussed in the following Sections.

The I_p=2 MA plasma without impurity is considered first. Figure 2(a) shows the time evolution of volume averaged electron density, $\langle n_e \rangle$, averaged electron temperature, $\langle T_e \rangle$, and averaged ion temperature, $\langle T_i \rangle$, with the weight of density profile. During the first one second, $\langle n_e \rangle$ is kept constant. After that, $\langle n_e \rangle$ begins to increase at a constant rate under the constant gas puffing rate. As $\langle n_e \rangle$ increases, $\langle T_e \rangle$ and $\langle T_i \rangle$ gradually decrease. The sudden decrease of $\langle T_e \rangle$ and $\langle T_i \rangle$ at the beginning of the numerical simulation is caused by the onset of sawtooth oscillation.

Figure 2(b) shows the time evolution of MHD activities, especially sawtooth oscillations and magnetic island formation by destabilized tearing modes. In this figure, the solid lines corresponding to $r_{1/1}$, $r_{3/2}$ and $r_{2/1}$ indicate the radial position of q=1, 1.5 and 2 surfaces, respectively. The dotted line r_c shows the radius within which helical flux, density and temperature are exchanged at the sawtooth crash. The dotted lines around the positions $r_{3/2}$ and $r_{2/1}$ indicate the width of (3,2) and (2,1) magnetic islands, respectively.

The time evolution of n_e, T_e and J_z profiles are shown in Fig. 3 . The n_e profile changes little during the density ramp up phase. The sawtooth oscillation occurs from the beginning of the numerical simulation. Within one third of minor radius in the plasma central region, the density and temperature profiles become almost flat due to the sawtooth crash. However, the m=2 tearing mode activity are weakly unstable before t=6.8 sec. From t=6.8 sec, the width of magnetic island due to the (2,1) tearing mode rapidly increases. With a short delay, the (3,2) island width begins to increase. The time when the (3,2) island width begins to increase coincides with the time when the (2,1) island width becomes maximum. The J_z profile does not change until $\langle n_e \rangle$ becomes very large.

Profiles of n_e, T_e and T_i at $\langle n_e \rangle$=7.1×10^{19} m^{-3} (t=3.0 sec), $\langle n_e \rangle$=1.69 × 10^{20} m^{-3} (t=8.4 sec) and $\langle n_e \rangle$=1.77×10^{20} m^{-3} (t=8.8 sec) are shown in Fig. 4 . In the high density regime, T_i is almost the same as T_e due to the large electron-ion equipartition energy transfer. In Fig. 4(b), T_e and T_i is locally flat around r=0.57 m and r=0.7 m due to the (3,2) and (2,1) magnetic islands.

In Fig. 4(c), these islands are overlapped each other. Although the numerical simulation can continue for t>8.8 sec, it is considered that the major disruption occurs at this time. The maximum electron density just

before the major disruption is $\langle n_e \rangle = 1.77 \times 10^{20}$ m^{-3}, which corresponds to $\langle n_e \rangle R/B_t = 11.8$. This maximum density is unrealistically higher than experimentally obtained density limit in $I_p = 2$ MA ohmically heated plasmas of JT-60 (see the operation limit of JT-60 ohmically heated plasma shown in Fig. 34 for reference).

In the low density phase, for example at $t=3.0$ sec, the dominant electron energy loss channel is the conduction loss. In the high density phase, for example at $t=8.4$ sec, on the other hand, it is electron-ion equipartition energy transfer from electrons to ions. As $\langle n_e \rangle$ increases the ion conduction loss increases because χ_i^{NC} has a positive density dependence. Also the recombination loss increases in the low edge temperature plasmas in the high density regime. Then the electron energy loss increases through the electron-ion equipartition energy transfer, and the electron temperature profile changes substantially. The change of T_e profile affects the plasma current profile through the plasma resistivity, which has a tendency to destabilize (2,1) tearing mode.

Once the large (2,1) magnetic island is formed, the current density gradient between the $q=1$ and $q=2$ resonant surface becomes large. Then the (3,2) tearing mode is destabilized and (3,2) magnetic island appears. Finally the (2,1) and (3,2) islands are overlapped. However, after the elapse of resistive skin time, the current density gradients at both the $q=1.5$ and $q=2$ resonant surface become small because of the flat T_e profile within the magnetic island. Then the tearing modes are stabilized and the magnetic islands disappear. This process repeats itself in the numerical simulation.

If there are substantial number of impurity ions in the core plasma, the radiation loss by impurity plays an important role in the electron energy balance. This energy loss causes much lower density limit than the case without impurity. The details are discussed in the following Sections.

4. Density Limit by Light Impurity Effects

In this Section, the density limit caused by light impurities such as carbon and oxygen is investigated. At first, the density limit of $I_p = 1$ MA plasma with $I_{imp} = 1$ % oxygen is studied. Here Z_{eff} is about 1.45 . Figure 5(a) shows time evolution of $\langle n_e \rangle$, $\langle n_i \rangle$, $\langle T_e \rangle$ and $\langle T_i \rangle$.

Figure 5(b) is the time evolution of ohmic heating power, P_{OH}, and the total radiation loss, P_{rad}^{total}, due to the oxygen impurity. Before $t=1.0$ sec, P_{rad}^{total} is about 25 % of P_{OH}. After $t=1.0$ sec, P_{rad}^{total} increases rapidly with increase of

before the major disruption is $\langle n_e \rangle = 1.77 \times 10^{20}$ m^{-3}, which corresponds to $\langle n_e \rangle R/B_t = 11.8$. This maximum density is unrealistically higher than experimentally obtained density limit in $I_p = 2$ MA ohmically heated plasmas of JT-60 (see the operation limit of JT-60 ohmically heated plasma shown in Fig. 34 for reference).

In the low density phase, for example at $t = 3.0$ sec, the dominant electron energy loss channel is the conduction loss. In the high density phase, for example at $t = 8.4$ sec, on the other hand, it is electron-ion equipartition energy transfer from electrons to ions. As $\langle n_e \rangle$ increases the ion conduction loss increases because χ_i^{NC} has a positive density dependence. Also the recombination loss increases in the low edge temperature plasmas in the high density regime. Then the electron energy loss increases through the electron-ion equipartition energy transfer, and the electron temperature profile changes substantially. The change of T_e profile affects the plasma current profile through the plasma resistivity, which has a tendency to destabilize (2,1) tearing mode.

Once the large (2,1) magnetic island is formed, the current density gradient between the $q = 1$ and $q = 2$ resonant surface becomes large. Then the (3,2) tearing mode is destabilized and (3,2) magnetic island appears. Finally the (2,1) and (3,2) islands are overlapped. However, after the elapse of resistive skin time, the current density gradients at both the $q = 1.5$ and $q = 2$ resonant surface become small because of the flat T_e profile within the magnetic island. Then the tearing modes are stabilized and the magnetic islands disappear. This process repeats itself in the numerical simulation.

If there are substantial number of impurity ions in the core plasma, the radiation loss by impurity plays an important role in the electron energy balance. This energy loss causes much lower density limit than the case without impurity. The details are discussed in the following Sections.

4. Density Limit by Light Impurity Effects

In this Section, the density limit caused by light impurities such as carbon and oxygen is investigated. At first, the density limit of $I_p = 1$ MA plasma with $I_{imp} = 1$ % oxygen is studied. Here Z_{eff} is about 1.45 . Figure 5(a) shows time evolution of $\langle n_e \rangle$, $\langle n_i \rangle$, $\langle T_e \rangle$ and $\langle T_i \rangle$.

Figure 5(b) is the time evolution of ohmic heating power, P_{OH}, and the total radiation loss, P_{rad}^{total}, due to the oxygen impurity. Before $t = 1.0$ sec, P_{rad}^{total} is about 25 % of P_{OH}. After $t = 1.0$ sec, P_{rad}^{total} increases rapidly with increase of

density. At t=2.0 sec P_{rad}^{total} is almost comparable to P_{OH}. P_{rad}^{total} continuously increases as the electron density. P_{OH} also increases due to increase of plasma resistivity because T_e decreases. Thus, after t=2.0 sec, P_{rad}^{total} keeps almost the same level as P_{OH}.

Figure 5(c) shows the time evolution of the location of $r_{1/1}$, r_c, $r_{3/2}$, $r_{2/1}$ and the width of (2,1) and (3,2) magnetic islands. It is seen $r_c \sim 1.1 r_{1/1}$. This is a little different from the flux inversion radius given by Kadomtsev; $r_c \sim \sqrt{2}$ $r_{1/1}$. Since the current peaking after the sawtooth collapse is very slow in the simulation, the increase of helical flux inside the radius of $r_{1/1}$ is also small. Thus the flux exchange between $q \leq 1$ and $q \geq 1$ is restricted in a narrow region during the minor disruption of sawtooth. Therefore the ratio $r_c/r_{1/1}$ may become small. As the density increases, the three resonant surfaces $r_{1/1}$, $r_{3/2}$, $r_{2/1}$ gradually move outward. At t=2.7 sec, the (2,1) island width suddenly increases and the (3,2) island width increases just after that. At t=3.2 sec these two islands are overlapped each other. The electron density at this time is $\langle n_e \rangle$=2.39×10^{19} m^{-3}, which corresponds to the density limit.

The time evolution of n_e, T_e and J_z profiles are shown in Fig. 6 . After t=1.0 sec, T_e and J_z in the peripheral region gradually decrease. Then at t=2.0 sec when P_{rad}^{total} is comparable to P_{OH}, the shrinkage of the T_e and J_z profiles take place. The current density gradient around the q=2 resonant surface becomes large and the (2,1) magnetic island is formed. As this magnetic island width becomes large, the current density gradient around the q=1.5 surface also becomes large, which causes the formation of the (3,2) magnetic island. Then these islands are overlapped and the major disruption occurs suddenly. The interaction between the (2,1) mode and the (1,1) mode is negligible in this case.

Figure 7 shows profiles of n_e, n_i, T_e, T_i and P_{rad}. At $\langle n_e \rangle$=1.72×10^{19} m^{-3} (t=2.0 sec), there are two peaks in the radiation loss profile, which correspond to the positions of T_e=50 eV and 300 eV. The temperature dependence of cooling rate in Fig. 1 shows two peaks at T_e=20 eV and 200 eV for the oxygen. The shift of maximum radiation cooling position to the higher T_e region is caused by the diffusion of impurity. The radiation loss profile is strongly localized at the plasma edge region. The intensity of outer peak is especially large. This radiation profile is the distinctive feature for the light impurity case. The ratio of P_{rad}^{total} to P_{OH} is about 0.38 . At this time, the (2,1) tearing mode is still stable.

At $\langle n_e \rangle$=2.35×10^{19} m^{-3} (t=3.3 sec) the electron temperature in the pe-

ripheral region cannot be supported any longer because the radiation loss overcomes the heat flow from the plasma central region to the edge region by conduction. Thus the electron temperature profile shrinks as shown in Fig. 7(b). The position of the maximum radiation loss moves about 15 cm inward. Outside this peak, a very low temperature plasma ($\sim$5 eV) exists. At this stage the (3,2) magnetic island also appears. Afterward, the (2,1) and (3,2) magnetic islands are overlapped (see Fig. 7(c)).

Figure 8 shows density profiles of oxygen in different charge states. The low charge state oxygen densities, mainly O^{3+}, O^{4+} and O^{5+}, which exist near the plasma surface generate the localized radiation loss. These low charge state oxygens begin to move inwardly when the shrinkage of electron temperature starts.

Next, the density limit of 2 MA plasma with oxygen of I_{imp}=1 % is investigated. Figures 9 and 10 show the time evolution of plasma parameters and profiles of n_e, T_e and J_z. Just before t=1.0 sec, P_{rad}^{total}/P_{OH} is about 0.2 . During the density ramp up, P_{rad}^{total} increases rapidly. At t=2.8 sec, P_{rad}^{total} becomes comparable to P_{OH}. Different from the I_p=1 MA case, the (2,1) tearing mode is always unstable through the density ramp up phase. Then at t=3.7 sec, the (2,1) and (3,2) magnetic islands are overlapped.

Figure 11 shows profiles of n_e, n_i, T_e, T_i and P_{rad}. Contrary to the I_p=1 MA case, the shrinkage of the electron temperature cannot be clearly seen. The position of maximum radiation loss locates outside the q=2 surface; r=0.85$\sim$0.90 m. However, radiation cooling in the plasma peripheral region does occur in the same way as the I_p=1 MA case. The current density gradient at q=2 becomes large and the (2,1) tearing mode is destabilized. The growth of (2,1) magnetic island makes large current density gradient at the q=1.5 surface. Then the (3,2) tearing mode is destabilized and the (3,2) magnetic island appears. At $\langle n_e \rangle \sim$4.3$\times 10^{19}$ m^{-3} (t=3.7 sec), P_{rad}^{total}/P_{OH} becomes 0.92 and the (2,1) and (3,2) modes become unstable simultaneously. In the next stage, these islands become overlapped. The density limit of I_p=2 MA case is larger than I_p=1 MA case because the ohmic heating power is increased for I_p=2 MA.

In the I_p=2 MA case, the wide flattening region of plasma current profile in the central region also makes large current density gradient at the q=2 surface. However, even if the central current flattening region is wide, the large width (2,1) island does not appear in the impurity free plasmas for t<6.8 sec (see Fig. 3(c)). It is clear that the increase of current density gradient at

the $q=2$ surface is affected by the radiation loss in the edge region more than by the central current density flattening due to the sawtooth oscillations.

Figure 12 shows density profiles of oxygen in different charge states. Since the edge temperature is higher than that of $I_p=1$ MA case, the low charge state oxygen are more localized near the plasma surface even at the high density regime.

Besides oxygen, carbon is also commonly observed impurity in tokamaks. Here $I_p=2$ MA plasma with $I_{imp}=6$ % carbon is studied. Figure 13 shows profiles of n_e, n_i, T_e, T_i and P_{rad} and carbon density in different charge states at $\langle n_e \rangle = 2.79 \times 10^{19}$ m^{-3}. Radiation loss profile is highly localized near the plasma surface. The density of C^{2+} and C^{3+}, which mainly contribute to the radiation loss, are localized near the plasma surface.

The impurity density in each charge state is calculated by eq.(11) taking into account of radial impurity flux. Now corona-equilibrium model is often referred to estimate the impurity density ratio in each charge state at a given temperature. Here the density limit is calculated by using the corona-equilibrium model and compared with results by the impurity diffusion model.

Figures 14 and 15 using the corona-equilibrium model correspond to Fig. 5 and Fig. 6, respectively. When $\langle n_e \rangle$ is less than 4.5×10^{19} m^{-3} or $t < 7.4$ sec, P_{rad}^{total} is much less than P_{OH}, MHD activity is weak comparing with Fig. 5 and the shrinkage of T_e and J_z profiles is not seen clearly. However, the central flat region by the sawtooth oscillation is smaller than that in the case of the impurity diffusion model. At $\langle n_e \rangle \sim 4.5 \times 10^{19}$ m^{-3}, (2,1) and (3,2) magnetic islands suddenly burst.

The difference between the corona-equilibrium model and the impurity diffusion model is highlighted by comparing Fig. 16, Fig. 17 and Fig. 7, Fig. 8. At $\langle n_e \rangle = 2.73 \times 10^{19}$ m^{-3} ($t=4.0$ sec), the profile of P_{rad} is quite different from the impurity diffusion model (see Fig. 7(c)). P_{rad} profile is not localized, rather broad in the bulk plasma. The reason can be inferred from the density profile of impurity. Figure 17(a) shows that there are only O^{8+}, O^{7+}, O^{6+} in the bulk plasma. Lower charge state oxygen are actually only seen at the mesh point corresponding to the plasma surface. They cannot move into the inner region because there is no impurity diffusion in the corona-equilibrium model.

In the impurity diffusion model, these low charge state oxygen spread into the bulk plasma and generate P_{rad} profile with finite spatial width (see Fig. 8). In the corona-equilibrium model, on the other hand, the local T_e value determines what kind of charge state oxygen exists. Thus the radiation loss

due to the low charge state oxygen impurity is really restricted at the plasma surface. In Figs. 16(a) and (b), the peak of radiation loss caused by low charge state oxygens can be seen at $r=0.95$ m.

The radiation loss power at the plasma central region in Fig. 16(a), $P_{rad}\sim10^4$ W/m^3, is as large as that in Fig. 7(c). That is, the distinctive difference between the corona-equilibrium model and the impurity diffusion model in the light impurity case is not the difference of P_{rad} profile but whether significant amount of P_{rad} caused by the low charge state oxygen exists in the edge region or not. At $\langle n_e \rangle=4.39\times10^{19}$ m^{-3} ($t=7.4$ sec, Fig. 16(b)), P_{rad} has another peak in the peripheral region ($r=0.8\sim0.9$ m). This is caused by the increase of O^{5+} in this region because T_e decreases as the increase of $\langle n_e \rangle$.

From $t=7.4$ sec to $t=7.6$ sec, O^{4+}, O^{3+}, O^{2+}, O^{1+} appear successively in the plasma edge region. The rapid increase of radiation loss by the appearance of these low charge state oxygen causes the decrease of T_e, which promotes further increase of radiation loss. This rapid increase of radiation loss makes the plasma current channel shrink inward very rapidly. Figure 16(c) shows a peaked P_{rad} profile just outside the $q=2$ surface. Then the current density gradients at $q=1.5$ and 2 are enhanced, and the (2,1) and (3,2) magnetic islands are overlapped.

The obtained density limit is $\langle n_e \rangle=4.48\times10^{19}$ m^{-3} by the corona-equilibrium model, which is about 1.9 times larger than the density limit by the impurity diffusion model and much larger than the density limit obtained experimentally in JT-60 ohmically heated plasmas.

It is considered that the corona-equilibrium model underestimates the density of low charge state oxygen and consequently the radiation loss. In the light impurity case, it is inappropriate to adopt the corona-equilibrium model for the estimation of impurity density.

5. Density Limit by Metal Impurity Effects

In this Section, the metal impurity case is studied. First of all, the density limit of $I_p=1$ MA plasma with $I_{imp}=0.05$ % titanium is examined. Titanium is the 22nd element. Here Z_{eff} is about 1.1 .

Figures 18 and 19 correspond to Figs. 5 and 6 for oxygen impurity case. After the onset of gas puffing, P_{rad}^{total} increases as $\langle n_e \rangle$. At $t=4.8$ sec, P_{rad}^{total} becomes comparable to P_{OH}. Both P_{rad}^{total} and P_{OH} continue increasing with keeping the relation $P_{rad}^{total}\sim P_{OH}$. Then at $t=6.8$ sec, (2,1) and (3,2) islands

due to the low charge state oxygen impurity is really restricted at the plasma surface. In Figs. 16(a) and (b), the peak of radiation loss caused by low charge state oxygens can be seen at $r=0.95$ m.

The radiation loss power at the plasma central region in Fig. 16(a), $P_{rad}{\sim}10^4$ W/m^3, is as large as that in Fig. 7(c). That is, the distinctive difference between the corona-equilibrium model and the impurity diffusion model in the light impurity case is not the difference of P_{rad} profile but whether significant amount of P_{rad} caused by the low charge state oxygen exists in the edge region or not. At $\langle n_e \rangle = 4.39 \times 10^{19}$ m^{-3} ($t=7.4$ sec, Fig. 16(b)), P_{rad} has another peak in the peripheral region ($r=0.8{\sim}0.9$ m). This is caused by the increase of O^{5+} in this region because T_e decreases as the increase of $\langle n_e \rangle$.

From $t=7.4$ sec to $t=7.6$ sec, O^{4+}, O^{3+}, O^{2+}, O^{1+} appear successively in the plasma edge region. The rapid increase of radiation loss by the appearance of these low charge state oxygen causes the decrease of T_e, which promotes further increase of radiation loss. This rapid increase of radiation loss makes the plasma current channel shrink inward very rapidly. Figure 16(c) shows a peaked P_{rad} profile just outside the $q=2$ surface. Then the current density gradients at $q=1.5$ and 2 are enhanced, and the (2,1) and (3,2) magnetic islands are overlapped.

The obtained density limit is $\langle n_e \rangle = 4.48 \times 10^{19}$ m^{-3} by the corona-equilibrium model, which is about 1.9 times larger than the density limit by the impurity diffusion model and much larger than the density limit obtained experimentally in JT-60 ohmically heated plasmas.

It is considered that the corona-equilibrium model underestimates the density of low charge state oxygen and consequently the radiation loss. In the light impurity case, it is inappropriate to adopt the corona-equilibrium model for the estimation of impurity density.

5. Density Limit by Metal Impurity Effects

In this Section, the metal impurity case is studied. First of all, the density limit of $I_p=1$ MA plasma with $I_{imp}=0.05$ % titanium is examined. Titanium is the 22nd element. Here Z_{eff} is about 1.1 .

Figures 18 and 19 correspond to Figs. 5 and 6 for oxygen impurity case. After the onset of gas puffing, P_{rad}^{total} increases as $\langle n_e \rangle$. At $t=4.8$ sec, P_{rad}^{total} becomes comparable to P_{OH}. Both P_{rad}^{total} and P_{OH} continue increasing with keeping the relation $P_{rad}^{total}{\sim}P_{OH}$. Then at $t=6.8$ sec, (2,1) and (3,2) islands

are overlapped. Figure 19 is similar to Fig. 6 .

Figures 20 and 21 are the profile of n_e, T_e, T_i, P_{rad} and titanium density in each charge state. Different from the light impurity case shown in Fig. 7, P_{rad} profile becomes much broader; it spreads from the half radius to the plasma edge region. The edge cooling by the titanium impurity gradually decreases the electron temperature in the region outside the $q=2$ surface.

The densities of Ti^{12+} at the half radius and Ti^{4+} at the plasma edge are substantial. The density of fully ionized titanium Ti^{22+} is very small because the central temperature of ohmically heated plasmas is fairly low. There are two peaks in the P_{rad} profile, which correspond to $Ti^{4+} \sim Ti^{6+}$ and $Ti^{10+} \sim Ti^{14+}$. Especially the outer peak which locates outside the $q=2$ surface is dominant. This peak moves inward as $\langle n_e \rangle$ increase and a very low T_e plasma appears in the plasma peripheral region. Then at $\langle n_e \rangle = 2.84 \times 10^{19}$ m^{-3} major disruption occurs. This metal impurity case also demonstrates that the edge cooling leads to the disruption.

Figures 22 and 23 shows the time evolution of the same quantities as shown in Figs. 18 and 19 in $I_p=2$ MA plasma with $I_{imp}=0.05$ % titanium. The (2,1) tearing mode is always unstable through the density ramp up. At $\langle n_e \rangle = 3.06 \times 10^{19}$ m^{-3} ($t=3.5$ sec), (2,1) and (3,2) island widths increase. However, they are not overlapped. P_{rad}^{total} increases as $\langle n_e \rangle$. However, the ratio P_{rad}^{total}/P_{OH} is utmost 0.65 during the density ramp up phase before $t=5.5$ sec when (2,1) and (3,2) islands are just overlapped.

Figures 24 and 25 shows profiles of n_e, T_e, P_{rad}, T_i and titanium density in each charge state. For almost the same $\langle n_e \rangle \sim 2.8 \times 10^{19}$ m^{-3} as shown in Figs. 20(c) and 4.24(a), the edge temperature of $I_p=2$ MA case is larger than that of $I_p=1$ MA case. Therefore the fraction of titanium density belonging to the low charge states is relatively smaller than that in the $I_p=1$ MA case.

P_{rad} is large in the region from the half radius to the plasma edge including both the $q=1.5$ and $q=2$ surfaces. The current channel shrinkage cannot be seen. However, the decrease of current density in the edge region due to the widely spread edge radiation cooling does change current density gradients at $q=1.5$ and $q=2$ surface, and results in the overlapping of (2,1) and (3,2) islands.

Next, the density limit of $I_p=1$ MA plasma with $I_{imp}=0.01$ % molybdenum is examined. Molybdenum is the 42nd element. Here Z_{eff} is about 1.03. Figures 26 and 27 show the time evolution of the same quantities as shown in Figs. 18 and 19 . In the density ramp up phase P_{rad}^{total} increases and after $t=3.6$ sec $P_{rad}^{total} \sim P_{OH}$. The T_e and J_z profiles begin to shrink at this time (see

Fig. 27).

Figures 28 and 29 show the profiles of n_e, T_e, T_i, P_{rad} and molybdenum density in each charge state. Different from oxygen or titanium, P_{rad} is dominant in the plasma central region where the ohmically heating power is also significant. In the edge region, there is peak of P_{rad}, which is caused by the low charge state molybdenum such as $Mo^{4+} \sim Mo^{10+}$. This peak locates at the electron temperature on the order of 50 eV. The density of molybdenum in the high charge state above Mo^{30+} is very low.

Although the radiation cooling is large in the plasma central region, the overlapping of (2,1) and (3,2) islands is mainly caused by the shrinkage of current channel due to the radiation loss in the edge region even in the metal impurity case. Comparing Fig. 28(c) with Fig. 7(c), it is found that the electron temperature profiles at the density limit are similar regardless of the impurity species.

Like the light impurity case, it is examined whether the corona- equilibrium model is applicable to the metal impurity case or not. The $I_p=1$ MA plasma with $I_{imp}=0.01$ % molybdenum is examined.

Figures 30 and 31 correspond to Figs. 14 and 15 for oxygen impurity case. Different from the oxygen case calculated by the corona-equilibrium model in which P_{rad}^{total} increases suddenly and T_e and J_z profiles collapse, P_{rad}^{total} becomes as large as P_{OH} ($t=4.2$ sec) before the overlapping of (2,1) and (3,2) islands and keeps increasing with $P_{rad}^{total} \sim P_{OH}$. Comparing Fig. 26 with Fig. 30, it is found that time evolution of plasma parameters is almost independent of the impurity models.

Figures 32 and 33 are the profiles of n_e, T_e, T_i, P_{rad} and molybdenum density in each charge state. At $\langle n_e \rangle = 2.43 \times 10^{19}$ m^{-3} ($t=3.0$ sec), P_{rad} shows the maximum near the plasma center. Another peak of P_{rad} does not exist in the edge region at this density. The reason is that the low charge state molybdenum densities $Mo^{1+} \sim Mo^{7+}$ are strongly localized at the plasma surface (see Fig. 33(a)) and does not contribute to the radiation loss.

At $\langle n_e \rangle = 2.87 \times 10^{19}$ m^{-3} ($t=4.2$ sec) when P_{rad}^{total} is comparable to P_{OH}, the low charge state molybdenum densities spread in the edge region because of the lower T_e than Fig. 33(a). Then P_{rad} profile has another peak in the edge region. At this time, by comparing Fig. 28(b) with Fig. 32(b), it is found that the overall P_{rad} profile is similar to that given by the impurity diffusion model.

Then the current channel begins to shrink and the (2,1) and (3,2) islands are overlapped at $\langle n_e \rangle = 3.08 \times 10^{19}$ m^{-3} ($t=4.8$ sec). The density limit of the

plasma with molybdenum impurity estimated by using the corona-equilibrium model is only about 10 % smaller than that by the impurity diffusion model, which is entirely different from the case of I_p=1 MA with I_{imp}=1 % oxygen.

Comparing Fig. 29(b) with Fig. 33(c) in the case of $\langle n_e \rangle \sim 3.1 \times 10^{19}$ m^{-3} it is found that the low charge state molybdenum densities $Mo^{4+} \sim Mo^{10+}$ in the impurity diffusion model are only slightly smaller than those in the corona-equilibrium model. Since $Mo^{4+} \sim Mo^{10+}$ contribute to P_{rad} dominantly in the plasma edge region, it is understandable that the density limits by these two models are similar.

This comparison suggests that for the metal impurity contaminated plasmas especially with high charge number impurity ions, the corona- equilibrium model is usable for the estimation of impurity charge state.

6. Comparison with Experimental Data of JT-60 Tokamak

When the impurity species and impurity content, I_{imp}, is fixed, the density limit increases as the plasma current. This is because the larger ohmic heating power can prevent the shrinkage of current channel which is caused by the imbalance between radiation loss and heating power.

The tokamak operational limit is described in the ($\langle n_e \rangle R/B_t$, q_a^{-1}) plane, which is so-called Hugill diagram. Here q_a is the safety factor at the plasma surface. The horizontal line, $\langle n_e \rangle R/B_t$, is usually called Murakami parameter. Originally, the line averaged electron density, $\bar{n}_e$, is adopted instead of the volume averaged one $\langle n_e \rangle$. $\bar{n}_e$ is larger than $\langle n_e \rangle$ by utmost 20 % in our calculations. In this Section, $\langle n_e \rangle$ is adopted for the Hugill diagram.

Figure 34 is the Hugill diagram. Numerical results and the JT-60 experimental data are shown by lines and closed symbols, respectively. The increase of plasma current or the reduction of impurity content immediately increases the density limit. The contamination of metal impurity strongly reduces the density limit even if the impurity content is very small. The case of 0.5 % oxygen content, which corresponds to the case of $Z_{eff} \sim 1.2$, is almost the minimum level of impurity content in JT-60 without major disruption. The experimentally obtained density limit quantitatively agrees with this line.

In discussing the density limit accurately, it is necessary to study the effect of impurity diffusion more carefully. As has been already pointed out in the Section 2.2, the impurity density profile is affected by the ratio C_A/D_A.

plasma with molybdenum impurity estimated by using the corona-equilibrium model is only about 10 % smaller than that by the impurity diffusion model, which is entirely different from the case of $I_p=1$ MA with $I_{imp}=1$ % oxygen.

Comparing Fig. 29(b) with Fig. 33(c) in the case of $\langle n_e \rangle \sim 3.1 \times 10^{19}$ m^{-3} it is found that the low charge state molybdenum densities $Mo^{4+} \sim Mo^{10+}$ in the impurity diffusion model are only slightly smaller than those in the corona-equilibrium model. Since $Mo^{4+} \sim Mo^{10+}$ contribute to P_{rad} dominantly in the plasma edge region, it is understandable that the density limits by these two models are similar.

This comparison suggests that for the metal impurity contaminated plasmas especially with high charge number impurity ions, the corona- equilibrium model is usable for the estimation of impurity charge state.

6. Comparison with Experimental Data of JT-60 Tokamak

When the impurity species and impurity content, I_{imp}, is fixed, the density limit increases as the plasma current. This is because the larger ohmic heating power can prevent the shrinkage of current channel which is caused by the imbalance between radiation loss and heating power.

The tokamak operational limit is described in the $(\langle n_e \rangle R/B_t, q_a^{-1})$ plane, which is so-called Hugill diagram. Here q_a is the safety factor at the plasma surface. The horizontal line, $\langle n_e \rangle R/B_t$, is usually called Murakami parameter. Originally, the line averaged electron density, $\bar{n}_e$, is adopted instead of the volume averaged one $\langle n_e \rangle$. $\bar{n}_e$ is larger than $\langle n_e \rangle$ by utmost 20 % in our calculations. In this Section, $\langle n_e \rangle$ is adopted for the Hugill diagram.

Figure 34 is the Hugill diagram. Numerical results and the JT-60 experimental data are shown by lines and closed symbols, respectively. The increase of plasma current or the reduction of impurity content immediately increases the density limit. The contamination of metal impurity strongly reduces the density limit even if the impurity content is very small. The case of 0.5 % oxygen content, which corresponds to the case of $Z_{eff} \sim 1.2$, is almost the minimum level of impurity content in JT-60 without major disruption. The experimentally obtained density limit quantitatively agrees with this line.

In discussing the density limit accurately, it is necessary to study the effect of impurity diffusion more carefully. As has been already pointed out in the Section 2.2, the impurity density profile is affected by the ratio C_A/D_A.

In the numerical results of this paper, these parameters are fixed at C_A=1 and D_A=0.4 m²sec⁻¹. Here, the value of C_A is changed to study its effect on the density limit.

Figure 35 shows the comparison of profiles of n_e, n_i, T_e, T_i, P_{rad} and carbon density in each charge state between C_A=1 case and C_A=4 case at $\langle n_e \rangle \sim 2.2 \times 10^{19}$ m⁻³ in the I_p=2 MA plasma with I_{imp}=6 % carbon. In this situation Z_{eff} is about 2.6 . Since the impurity density profile is more peaked in C_A = 4 case, the low charge state carbon densities C^{3+} or C^{2+} which cause the radiation cooling are much smaller in the edge region comparing with C_A=1 case. Therefore, P_{rad}^{total} of the C_A=1 case is about 2.9 times larger than the C_A=4 case at the same density. As a result, the density limit of C_A=4 case becomes about twice as large as that of C_A=1 case.

The similar results is obtained in the oxygen-contaminated plasma. Figure 36 shows the comparison of profiles of n_e, n_i, T_e, T_i, P_{rad} and oxygen density in each charge state between C_A=1 case and C_A=4 case at $\langle n_e \rangle \sim 3.0 \times 10^{19}$ m⁻³ in the I_p = 2 MA plasma with I_{imp}=2 % oxygen. In this situation Z_{eff} is about 1.85 . The low charge state oxygen densities O^{5+} or O^{4+} in C_A=4 case are much smaller than those in the C_A=1 case. Thus P_{rad}^{total} of C_A=4 case is about 40 % less than the C_A=1 case. Accordingly the density limits of C_A=2, 3 and 4 cases are 30 %, 60 % and 83% larger than that of C_A=1 case, respectively.

It is found that the density limit in the case of light impurity such as oxygen and carbon is affected by C_A.

Next the metal impurity case is examined. Figure 37 shows the comparison of profiles of n_e, T_e, T_i, P_{rad} and titanium density in each charge state between C_A=1 case and C_A=2 case at $\langle n_e \rangle \sim 2.7 \times 10^{19}$ m⁻³ in the I_p=2 MA plasma with I_{imp}= 0.05 % titanium. In this situation Z_{eff} is about 1.1 .

The titanium densities in the low charge state, $Ti^{1+} \sim Ti^{8+}$, are somewhat smaller in C_A=2 case comparing with C_A=1 case. However, different from the light impurity case the total radiation loss of C_A=2 case is almost the same as that of C_A=1 case, since the radiation loss is not determined only by these low charge state titanium densities. Thus the density limit of C_A=2 case is only 1 % smaller than that of C_A=1 case.

I_p=2 MA case with I_{imp}=0.05 % titanium are also examined to compare C_A=1 case with C_A=2 case. The results are shown in Fig. 38 for $\langle n_e \rangle \sim 2.9 \times 10^{19}$ m⁻³. In this case, the radiation loss is almost the same between C_A=1 case and C_A=2 case. Thus the density limit of C_A=2 case is only 9 % larger than that of C_A=1 case.

In the metal impurity case, it is considered that the effect of C_A on the density limit is small. The changes of density limit according to C_A value is summarized in Fig. 39 .

The value C_A should be carefully chosen to reproduce the spatial profile of radiation loss and effective charge number, which are measured by the bolometer array and the visible bremsstrahlung detector array, respectively.

7. Conclusion

Major disruptions in the high density regime of ohmically heated plasmas have been studied by using the one dimensional tokamak transport code including the impurity diffusion equation, the sawtooth oscillation model and the magnetic island evolution model.

Since the ionization energy of the light impurities such as carbon and oxygen is generally low, they become fully ionized except for the plasma peripheral region in case of the JT-60 plasma parameters. The radiation loss, which is mainly caused by the low charge state carbon or oxygen, becomes fairly localized at the plasma peripheral region. The central region is not affected by the radiation loss if there is no strong inward flow velocity of impurity.

On the other hand, the ionization energy of the heavy impurities or the metal impurities such as titanium and molybdenum is significantly higher than that of light impurities. Therefore they cannot reach the fully ionized state in the ohmically heated plasmas of large tokamaks in which the central T_e reaches 2∼3 keV. Thus, metal impurities in the different charge state spread in the whole plasma region. The radiation loss profile is not localized at a specific region and becomes broad one.

Although the radiation loss profile is entirely different between the light impurity cases and the metal impurity cases, the process toward the density limit disruption is considered the same. It is related to the fact that the increase of density accompanies the increase of radiation loss. When the total radiation loss becomes comparable to the ohmic heating power, the plasma current channel usually begins to shrink. It does not matter whether the current channel shrinks from the plasma surface gradually as shown in the light impurity cases or the plasma current profile changes in a wide region between the half radius and the plasma surface as shown in the metal impurity cases.

At first, the current density gradient at $q=2$ surface becomes large and the (2,1) tearing mode is destabilized. Then the (2,1) magnetic island starts

In the metal impurity case, it is considered that the effect of C_A on the density limit is small. The changes of density limit according to C_A value is summarized in Fig. 39 .

The value C_A should be carefully chosen to reproduce the spatial profile of radiation loss and effective charge number, which are measured by the bolometer array and the visible bremsstrahlung detector array, respectively.

7. Conclusion

Major disruptions in the high density regime of ohmically heated plasmas have been studied by using the one dimensional tokamak transport code including the impurity diffusion equation, the sawtooth oscillation model and the magnetic island evolution model.

Since the ionization energy of the light impurities such as carbon and oxygen is generally low, they become fully ionized except for the plasma peripheral region in case of the JT-60 plasma parameters. The radiation loss, which is mainly caused by the low charge state carbon or oxygen, becomes fairly localized at the plasma peripheral region. The central region is not affected by the radiation loss if there is no strong inward flow velocity of impurity.

On the other hand, the ionization energy of the heavy impurities or the metal impurities such as titanium and molybdenum is significantly higher than that of light impurities. Therefore they cannot reach the fully ionized state in the ohmically heated plasmas of large tokamaks in which the central T_e reaches 2~3 keV. Thus, metal impurities in the different charge state spread in the whole plasma region. The radiation loss profile is not localized at a specific region and becomes broad one.

Although the radiation loss profile is entirely different between the light impurity cases and the metal impurity cases, the process toward the density limit disruption is considered the same. It is related to the fact that the increase of density accompanies the increase of radiation loss. When the total radiation loss becomes comparable to the ohmic heating power, the plasma current channel usually begins to shrink. It does not matter whether the current channel shrinks from the plasma surface gradually as shown in the light impurity cases or the plasma current profile changes in a wide region between the half radius and the plasma surface as shown in the metal impurity cases.

At first, the current density gradient at $q=2$ surface becomes large and the (2,1) tearing mode is destabilized. Then the (2,1) magnetic island starts

to grow. When the width of (2,1) island becomes sufficiently large, the current density gradient at $q=1.5$ surface becomes large. Then (3,2) tearing mode is destabilized and the (3,2) magnetic island grows in addition to the (2,1) magnetic island. When the (2,1) and (3,2) islands are overlapped, major disruption occurs due to rapid energy loss by destruction of magnetic surfaces.

In the large plasma current case, for example $I_p=2$ MA, the wide flat region of plasma current profile appears in the central region by the sawtooth oscillation which also makes large current density gradient at the $q=2$ surface. However, the increase of the current density gradient at $q=2$ surface is affected by the edge cooling due to the radiation loss much more than by the central current density flattening. When the plasma current becomes much larger, for example $q(a)=2\sim2.5$, the sawtooth induced current density flattening plays a role in triggering the major disruption.

The numerically obtained Hugill diagram quantitatively agrees well with that obtained in the JT-60 ohmically heated plasmas. The reduction of impurity content, especially the reduction of metal impurity content, is important for the high density operation of ohmically heated plasmas.

The corona-equilibrium model underestimates the densities of low charge state impurities which exist near the plasma surface. Therefore, the density limit is overestimated in the light impurity cases because the radiation loss is determined mainly by these low charge state impurities. It seems inappropriate to adopt the corona-equilibrium model to evaluate the radiation loss due to the light impurities. In the metal impurity case, on the other hand, the density limit by the corona-equilibrium model is almost the same as that obtained by the impurity diffusion model. The reason is that the radiation loss of metal impurity is determined not only by the low charge state but also the high charge state. Therefore corona-equilibrium model is effective to evaluate the radiation loss profile in the metal impurity case.

The density limit of light impurity is also affected by C_A value given by eq.(14). The larger C_A accompanies the larger density limit, because the ratio of the impurity density in the low charge state to the total impurity density decreases, and therefore the radiation loss decreases as C_A increases. In the metal impurity, on the other hand, C_A affects the density limit very little. In the JT-60 experiments, it is necessary to evaluate C_A precisely particularly for light impurities such as carbon and oxygen.

The simulation results presented in this paper are carried out by assuming the gas puffing from the plasma wall. The density profile is considerably flat. In

the JT-60 experiments with pellet injection, the density profile becomes highly peaked with a pedestal just after the pellet injection.[25] Since the edge density does not change, high density plasma becomes possible without increasing radiation loss. This is consistent with simulation results in this paper that the edge radiation loss causes the major disruption through the shrinkage of plasma current. In order to achieve the high density operation of ITER without major disruption, reduction of edge electron density is essential.

Acknowledgments

Authors acknowledge Drs. M. Nagami, R. Yoshino, S. Ishida, M . Kikuchi, H. Yoshida, O. Naito, Y. Koide, M. Sato, T. Sugie, K. Nagashima, K. Itami and N. Hosogane for fruitful discussion. Continuous encouragement by Dr. H. Kishimoto is also acknowledged.

the JT-60 experiments with pellet injection, the density profile becomes highly peaked with a pedestal just after the pellet injection.[25] Since the edge density does not change, high density plasma becomes possible without increasing radiation loss. This is consistent with simulation results in this paper that the edge radiation loss causes the major disruption through the shrinkage of plasma current. In order to achieve the high density operation of ITER without major disruption, reduction of edge electron density is essential.

Acknowledgments

References

[1] ITER Physics Committee, *ITER Physics Committee Meeting, Naka* (1994).

[2] N. R. Sauthoff, I. S. von Goeler and W. Stodiek, Nucl. Fusion **18** (1978) 1445.

[3] M. Murakami, J. D. Callen and L. A. Berry, Nucl. Fusion **16** (1976) 347.

[4] S. J. Fielding, J. Hugill, G. McCracken, J. W. M. Paul, P. Prentice and P. E. Stott, Nucl. Fusion **17** (1977) 1382.

[5] H. P. Furth, P. H. Rutherford and H. Selberg, Phys. Fluids **16** (1973) 1054.

[6] T. Hirayama, K. Shimizu, K. Tani, H. Shirai and M. Kikuchi, Experimental Transport Analysis Code System in JT-60, JAERI-M Report 88-043, Japan Atomic Energy Research Institute (1988).

[7] S. M. Kaye, F. M. Levinton, R. Hatcher, R. Kaita, C. Kessel, B. LeBlanc, D. C. McCune and S. Paul, Phys. Fluids B **4** (1992) 651.

[8] A. A. Ware, Phys. Rev. Lett. **25** (1970) 15.

[9] W. Feneberg, Nucl. Fusion **29** (1989) 1117.

[10] G. Fussmann, A. R. Field, A. Kallenbach, K. Krieger and K.-H. Steuer, Plasma Phys. Control. Fusion **33** (1991) 1677.

[11] F. Wagner, M. Bessenrodt-Weberpals, L. Giannone, A. Kallenbach, K. McCormick et al., Determination of Impurity Transport Coefficients by Sinusoidal Modulated Gas Puffing, *Proc. 17th Eur. Conf. on Controlled Fusion and Plasma Physics, Amsterdam, Netherlands, 1990*, Vol. 3 (1990) 1431.

[12] R. C. Isler and E. C. Crume, Phys. Rev. Lett. **41** (1978) 1296.

[13] P. E. Post, R. V. Jensen, C. B. Tarter, W. H. Grasberger and W. A. Lokke, Steady-state Radiative Cooling Rates for Low-density High-temperature Plasmas, At. Data Nucl. Data Tables **20** (1977) 397.

[14] M. Itoh, T. Yabe and S. Kiyokawa, Phys. Rev. A **35** (1987) 233.

[15] G. D. Hobbs and J. A. Wesson, Plasma Phys. **9** (1967) 85.

[16] D. Bohm et al., The Characteristics of Electrical Discharges in Magnetic Fields, National Nuclear Energy Series. McGraw-Hill Book Company Inc., New York (1949).

[17] L. Spitzer Jr., Phys. Fluids **3** (1960) 659.

[18] G. F. Matthews, P. C. Stangeby and P. J. Sewell, J. Nucl. Mater. **145-147** (1987) 220.

[19] B. V. Waddel, M. N. Rosenbluth, D. A. Monticello and R. B. White, Nucl. Fusion **16** (1976) 528.

[20] B. B. Kadomtsev, Sov. J. Plasma Phys. **1** (1975) 389.

[21] P. H. Rutherford, Phys. Fluids **16** (1973) 1903.

[22] R. B. White, D. A. Monticello, M. N. Rosenbluth and B. V. Waddell, Phys. Fluids **20** (1977) 800.

[23] B. Carreras, H. R. Hicks, J. A. Holmes and B. V. Waddell, Phys. Fluids **23** (1980) 1811.

[24] H. Vernickel and J. Bohdamsky, Nucl. Fusion **18** (1978) 1467.

[25] Y. Kamada, R. Yoshino, M. Nagami, T. Ozeki, T. Hirayama, H. Shirai, et al., Nucl. Fusion **30** (1989) 1785.
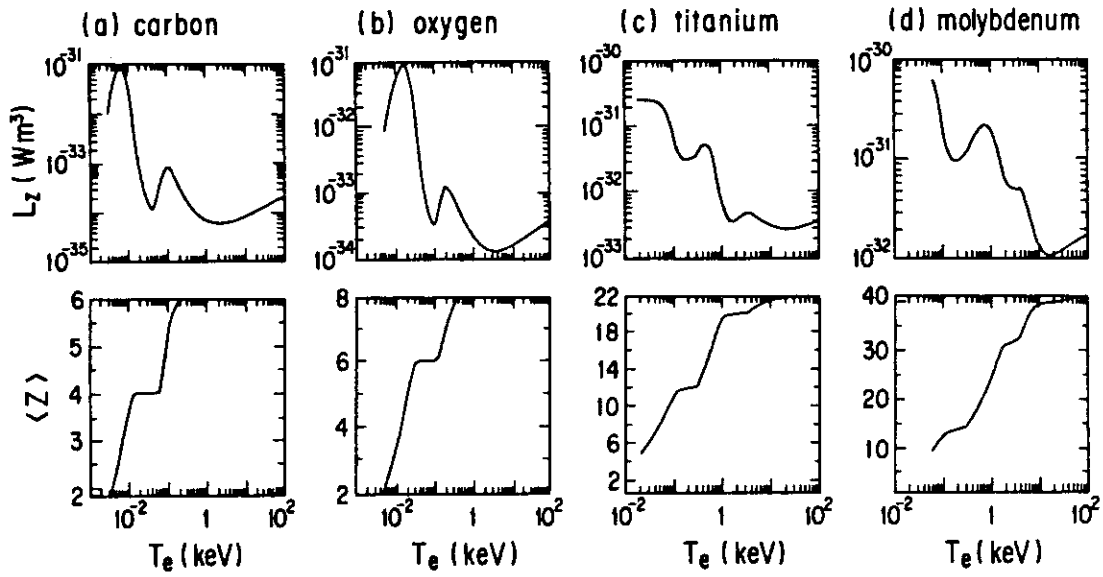
Fig. 1 The radiative cooling rate, L_Z, and the average charge state, $\langle Z \rangle$, as a function of T_e for typical impurities .[13]
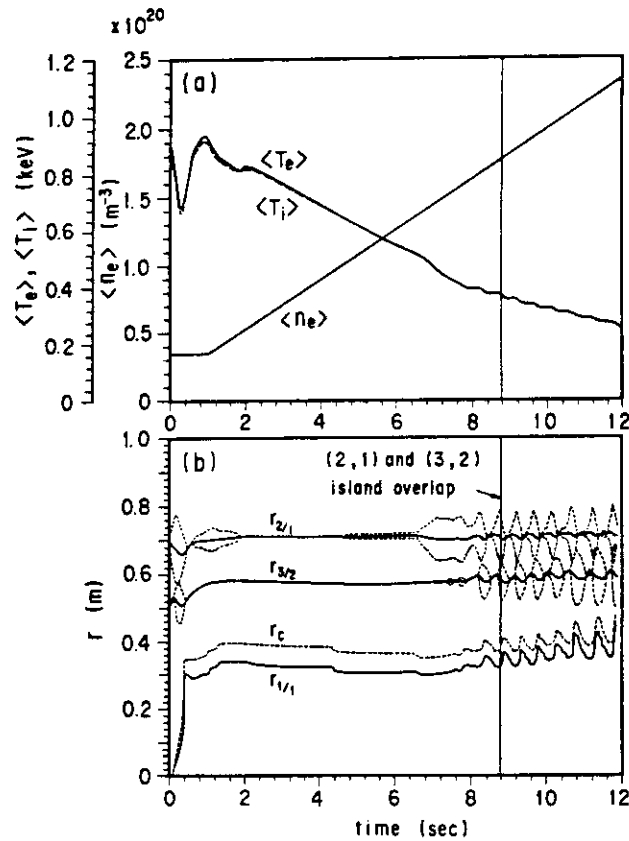
Fig. 2 Time evolution of plasma parameters in $I_p=2$ MA plasma without impurity.
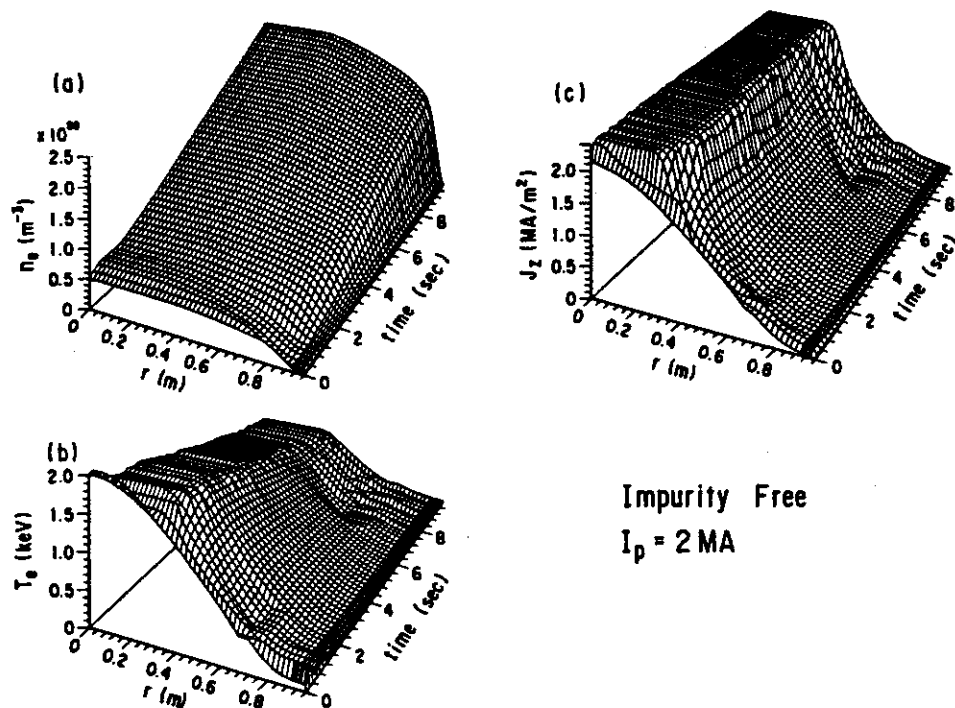
Fig. 3 Time evolution of n_e, T_e and J_z profiles in $I_p=2$ MA plasma without impurity.
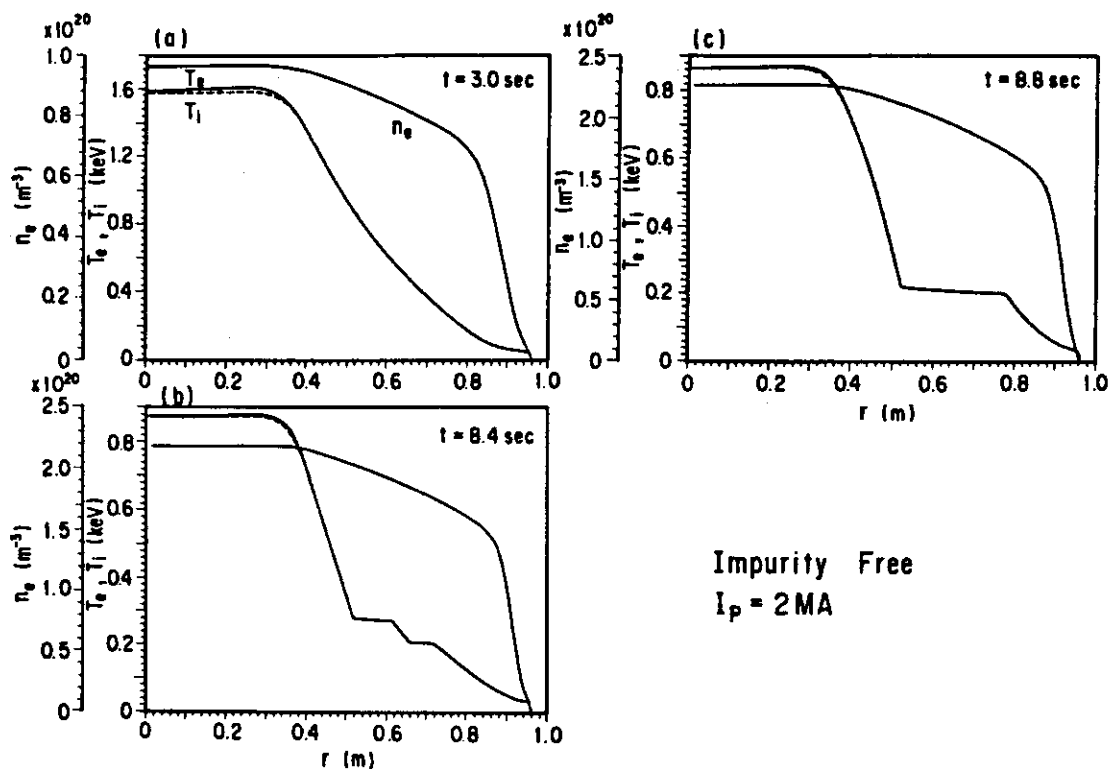
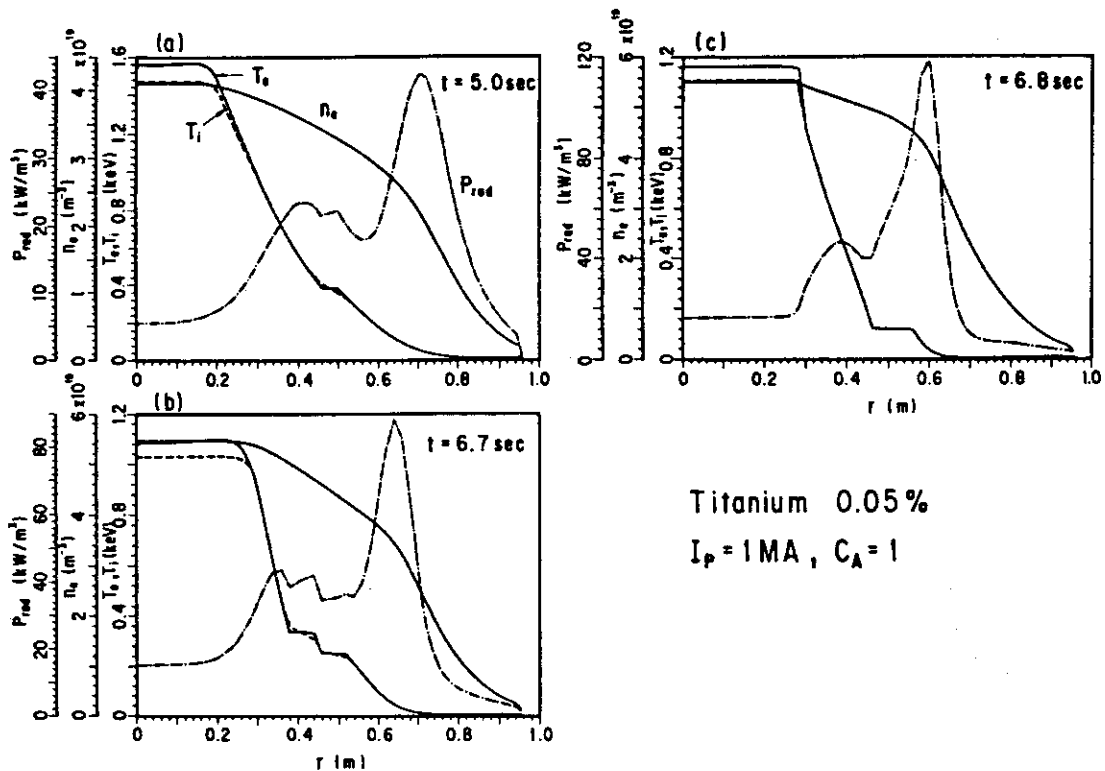**Fig. 4** Profiles of n_e, T_e, T_i and P_{rad} at $\langle n_e \rangle = 7.1 \times 10^{19}$ m^{-3} (t=3.0 sec), $\langle n_e \rangle = 1.69 \times 10^{20}$ m^{-3} (t=8.4 sec) and $\langle n_e \rangle = 1.77 \times 10^{20}$ m^{-3} (t=8.8 sec) in $I_p=2$ MA plasma without impurity.
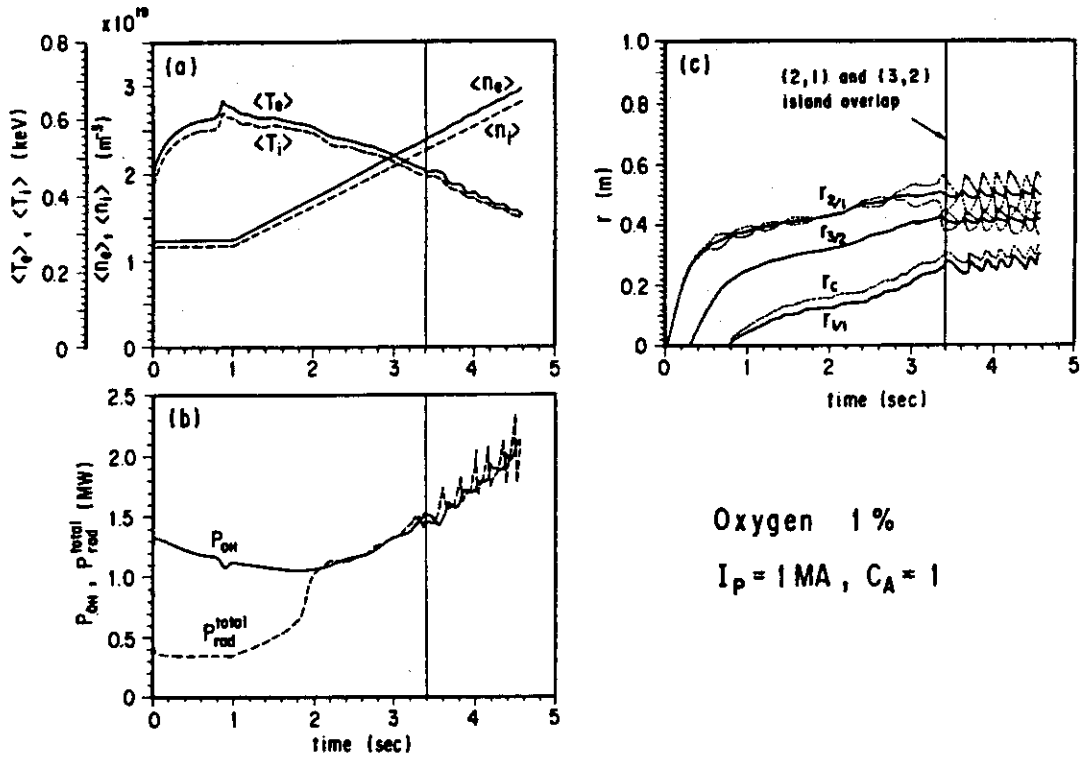
Fig. 5 Time evolution of plasma parameters in $I_p=1$ MA plasma with 1 % oxygen.
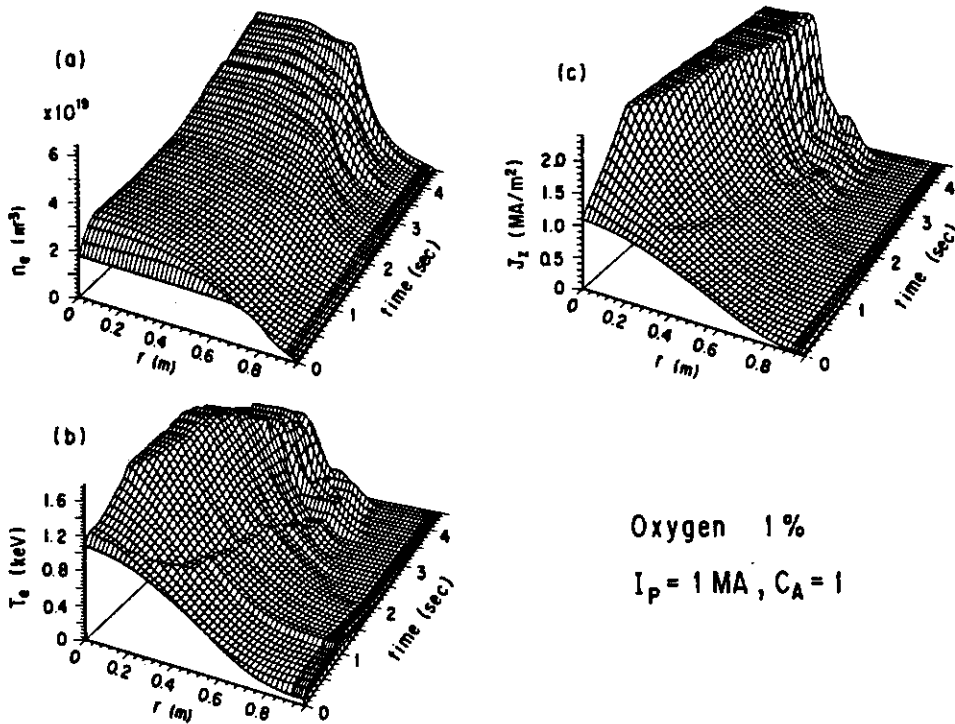
Fig. 6 Time evolution of n_e, T_e and J_z profiles in $I_p=1$ MA plasma with 1 % oxygen.
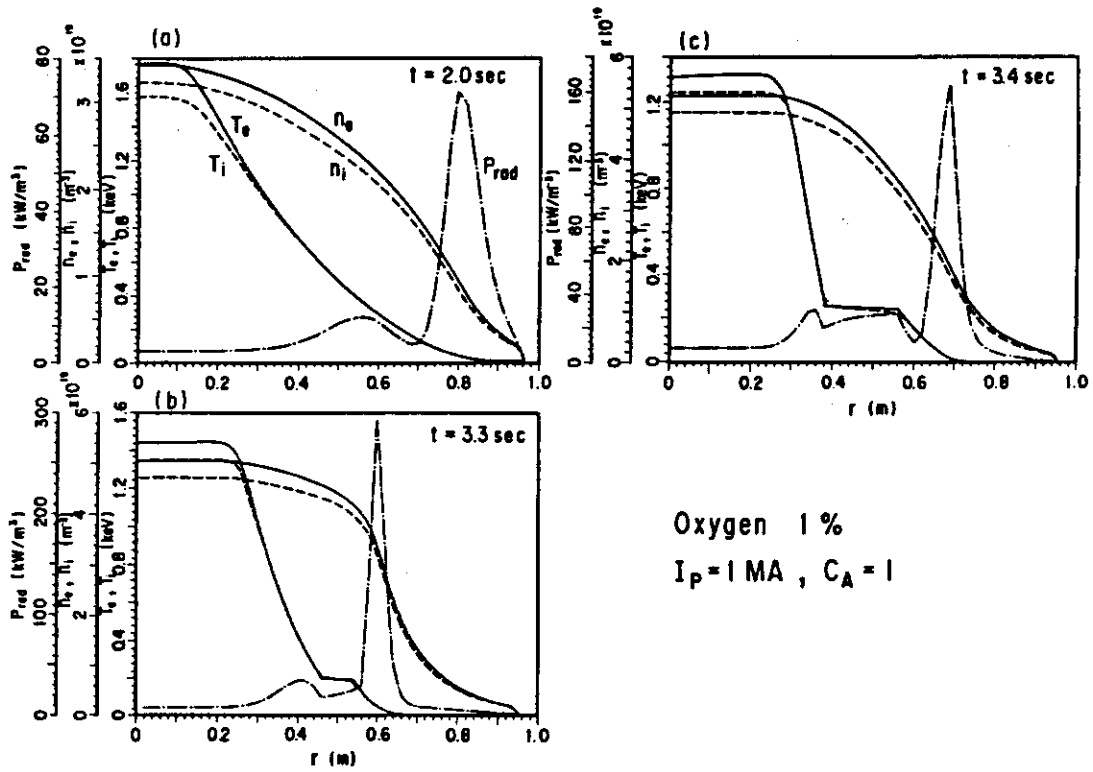
Fig. 7 Profiles of n_e, n_i, T_e, T_i and P_{rad} at $\langle n_e \rangle = 1.72 \times 10^{19}$ m^{-3} $(t=2.0$ sec), $\langle n_e \rangle = 2.35 \times 10^{19}$ m^{-3} $(t=3.3$ sec) and $\langle n_e \rangle = 2.39 \times 10^{19}$ m^{-3} $(t=3.4$ sec) in $I_p = 1$ MA plasma with 1 % oxygen.
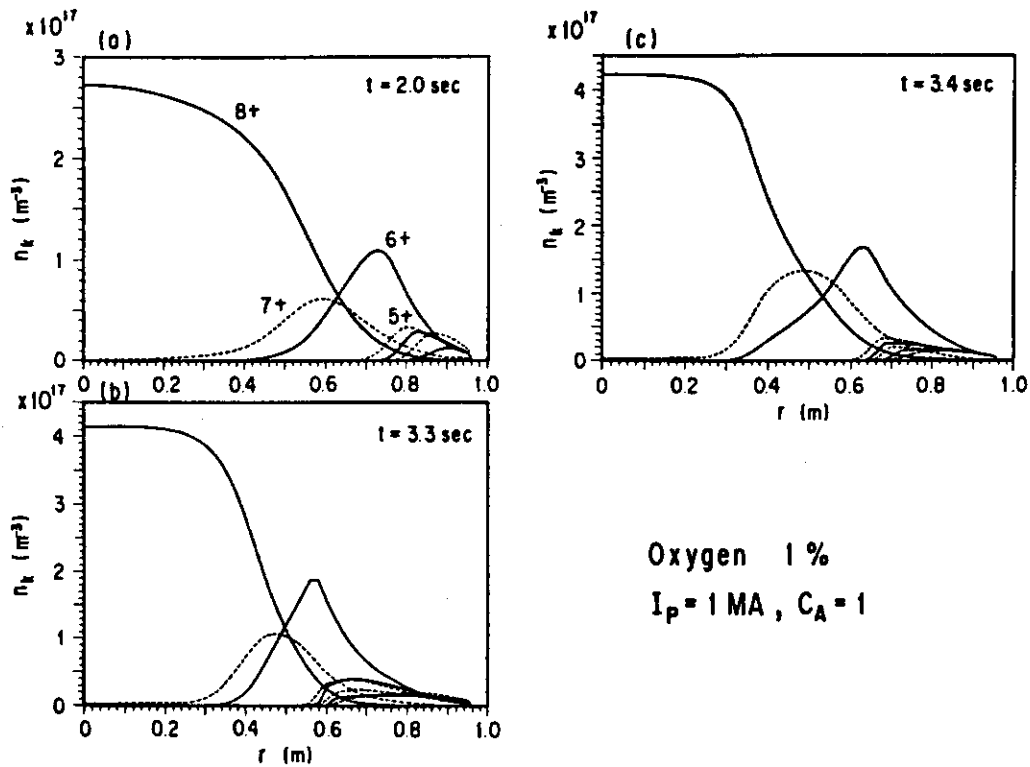
Fig. 8 Profiles of oxygen density n_k $(k=1, 2, \cdots, 8)$ at $t=2.0$, 3.3 and 3.4 sec in $I_p = 1$ MA plasma with 1 % oxygen.
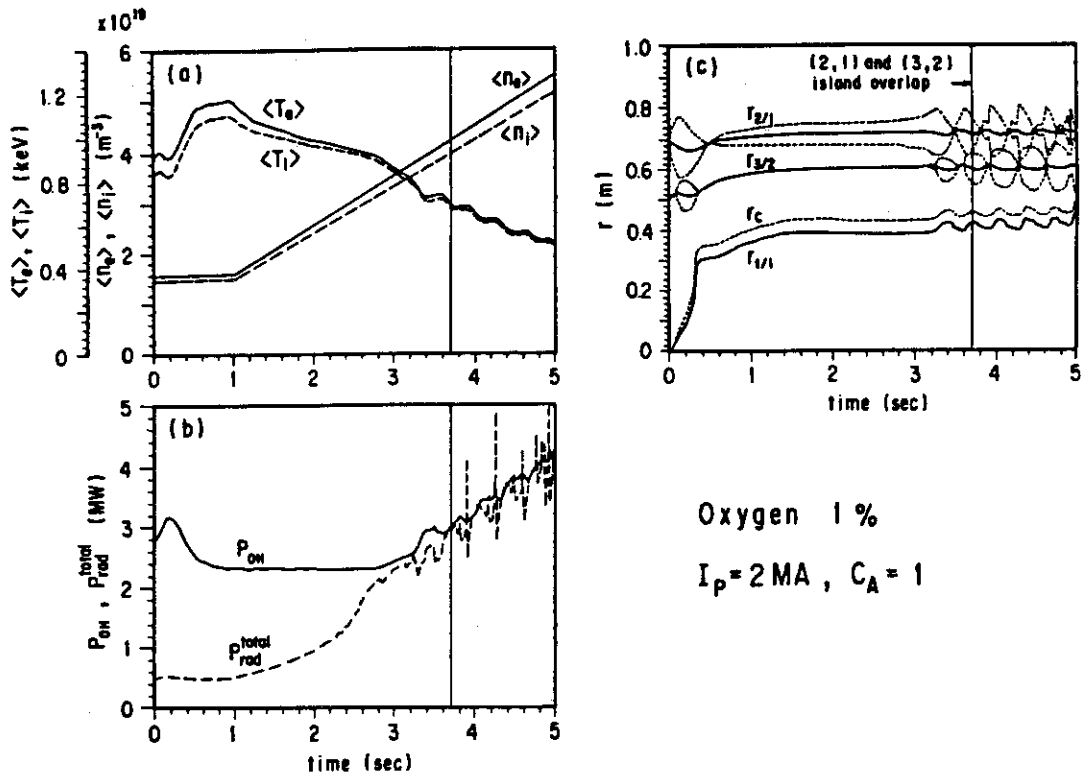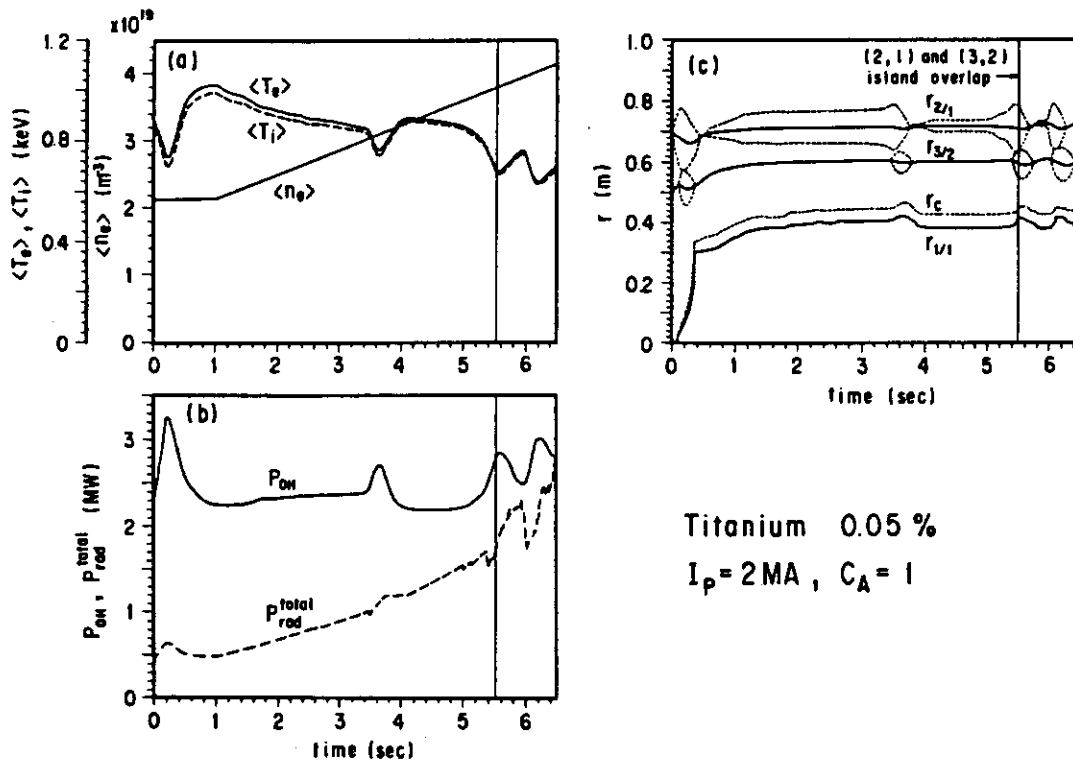
Fig. 9   Time evolution of plasma parameters in $I_p=2$ MA plasma with 1 % oxygen.
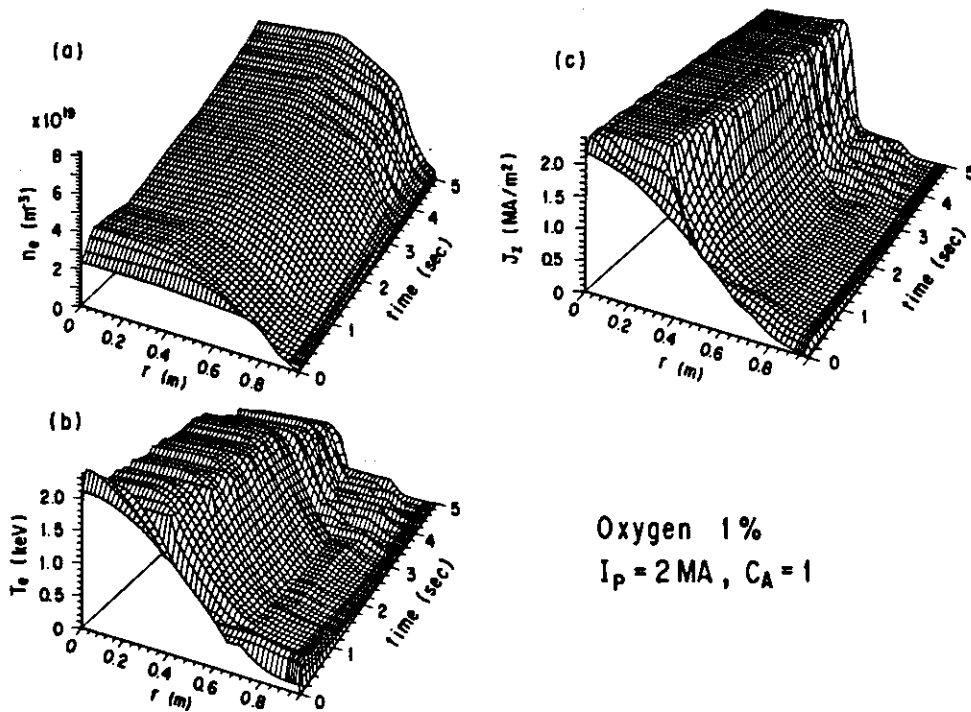
Fig. 10   Time evolution of n_e, T_e and J_z profiles in $I_p=2$ MA plasma with 1 % oxygen.
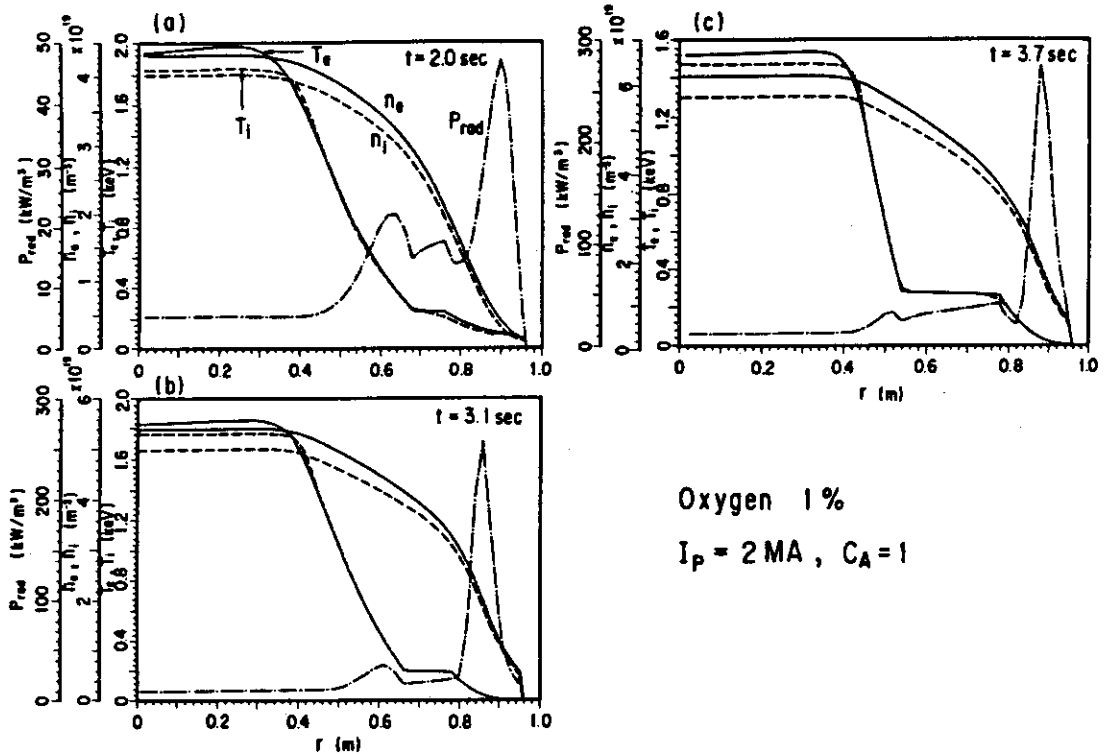
Fig. 11   Profiles of n_e, n_i, T_e, T_i and P_{rad} at $\langle n_e \rangle = 2.60 \times 10^{19}$ m^{-3} $(t=2.0$ sec$)$, $\langle n_e \rangle = 3.67 \times 10^{19}$ m^{-3} $(t=3.1$ sec$)$ and $\langle n_e \rangle = 4.25 \times 10^{19}$ m^{-3} $(t=3.7$ sec$)$ in $I_p = 2$ MA plasma with 1 % oxygen.
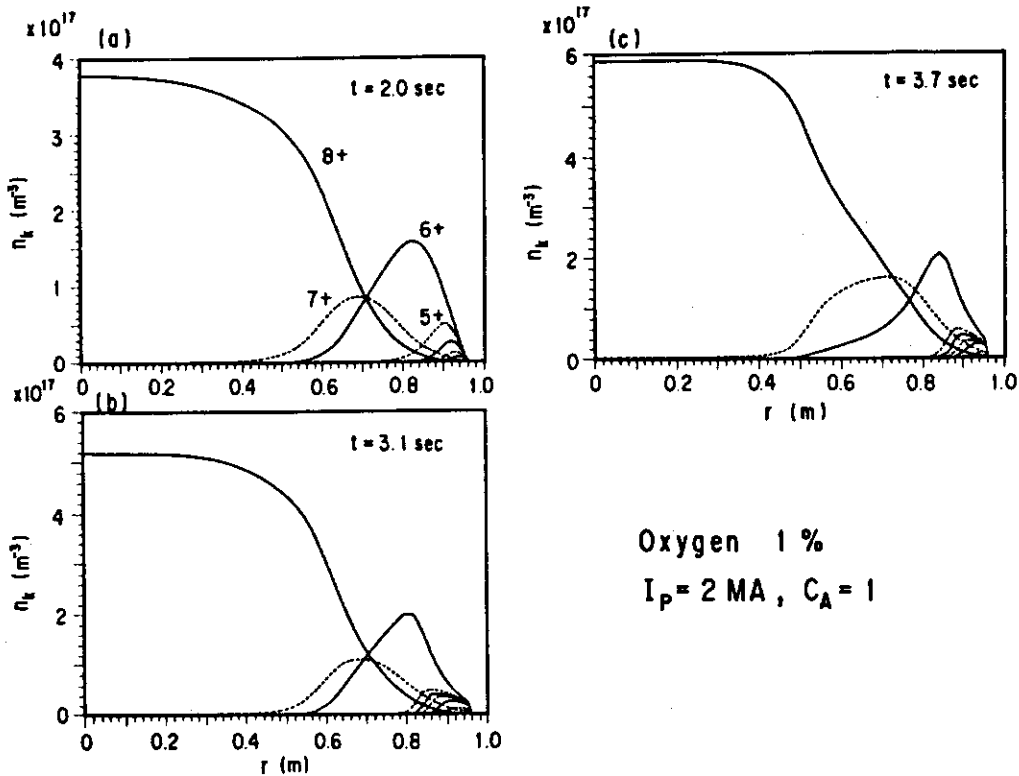
Fig. 12   Profiles of oxygen density n_k $(k=1, 2, \cdots, 8)$ at $t=2.0$, 3.1 and 3.7 sec in $I_p = 2$ MA plasma with 1 % oxygen.
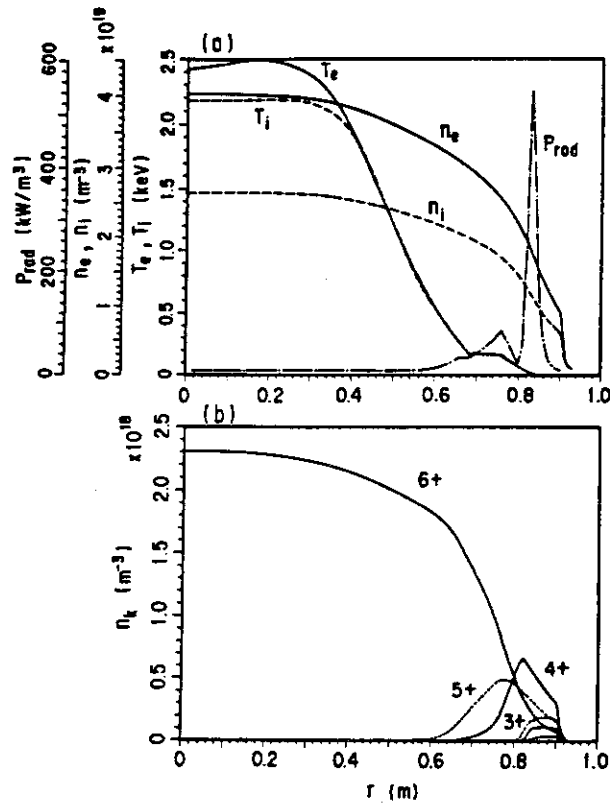
Fig. 13 Profiles of n_e, n_i, T_e, T_i, P_{rad} and carbon density n_k (k=1, 2, ···, 6) at $\langle n_e \rangle = 2.79 \times 10^{19}$ m^{-3} in $I_p = 2$ MA plasma with 6 % carbon.

Oxygen 1 %
$I_p = 1$ MA , $C_A = 1$
corona-equilibrium model
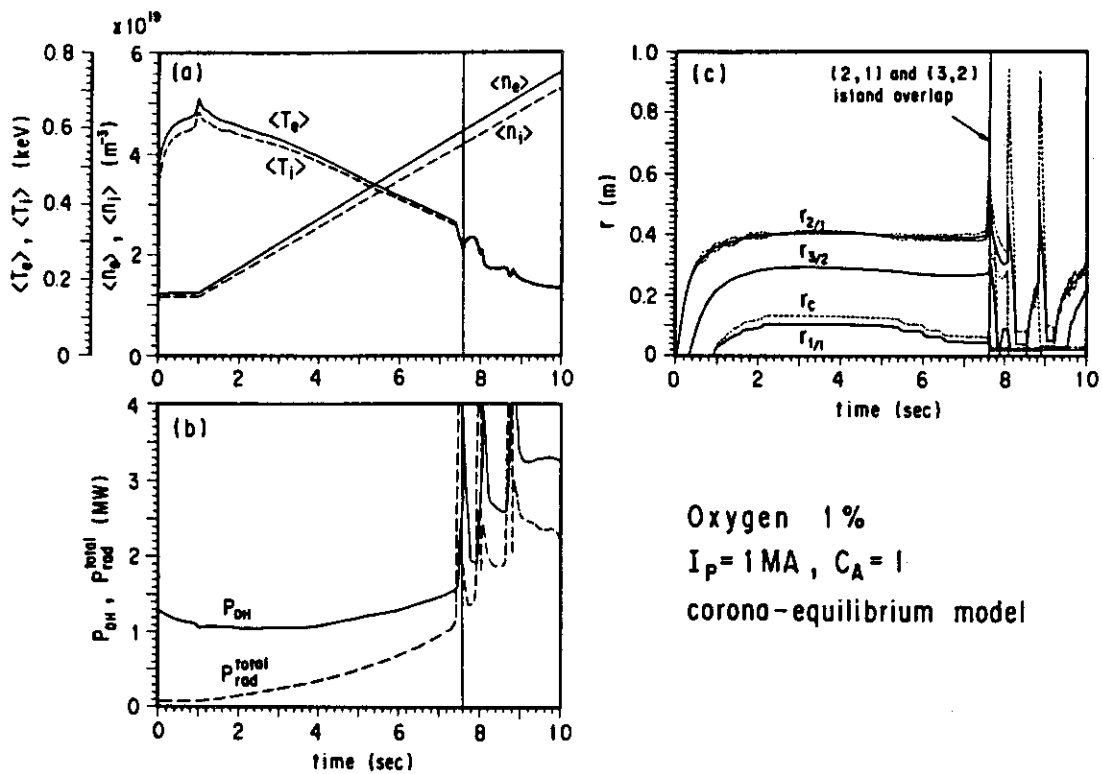
Fig. 14 Time evolution of plasma parameters in $I_p = 1$ MA plasma with 1 % oxygen. The corona-equilibrium model is assumed.
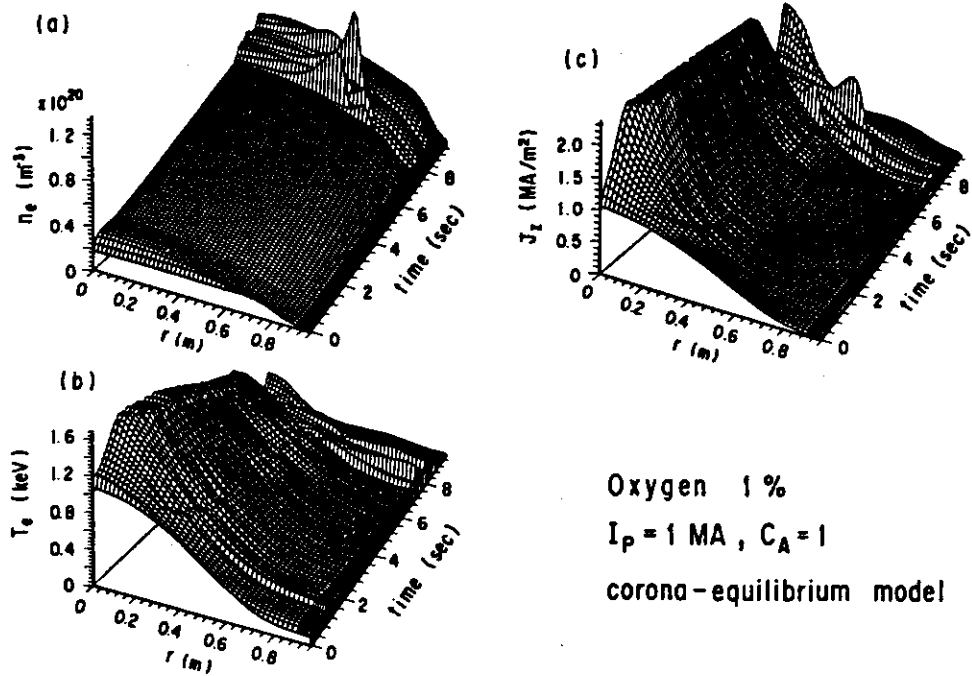
Fig. 15   Time evolution of n_e, T_e and J_z profiles in $I_p=1$ MA plasma with 1 % oxygen. The corona-equilibrium model is assumed.
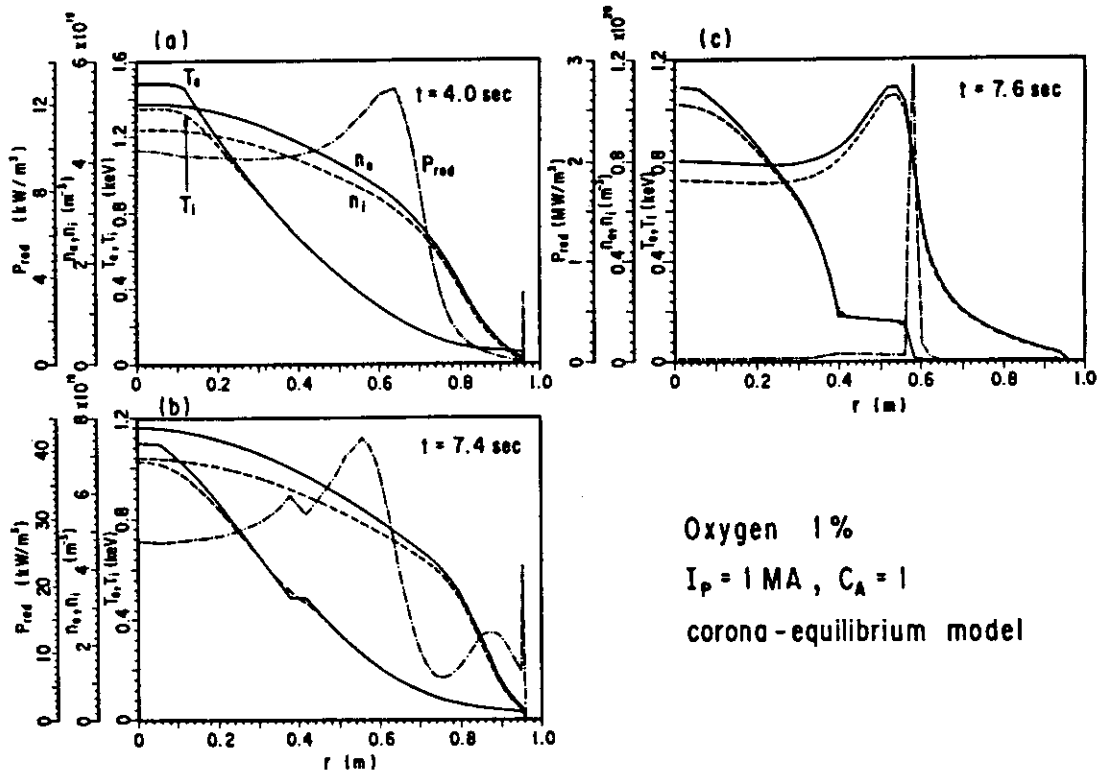
Fig. 16   Profiles of n_e, n_i, T_e, T_i and P_{rad} at $\langle n_e \rangle = 2.73 \times 10^{19}$ m^{-3} ($t=4.0$ sec), $\langle n_e \rangle = 4.39 \times 10^{19}$ m^{-3} ($t=7.4$ sec) and $\langle n_e \rangle = 4.48 \times 10^{19}$ m^{-3} ($t=7.6$ sec) in $I_p=1$ MA plasma with 1 % oxygen. The corona-equilibrium model is assumed.
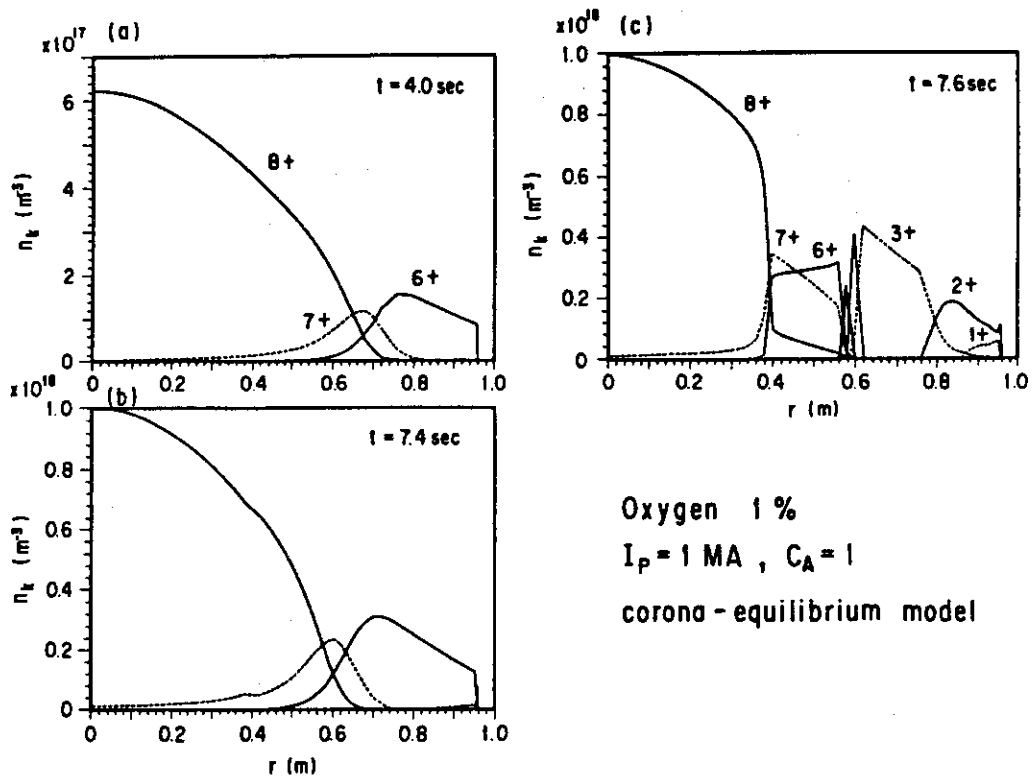
Fig. 17   Profiles of oxygen density n_k (k=1, 2, ···, 8) at t=4.0, 7.4 and 7.6 sec in I_p=1 MA plasma with 1 % oxygen. The corona-equilibrium model is assumed.
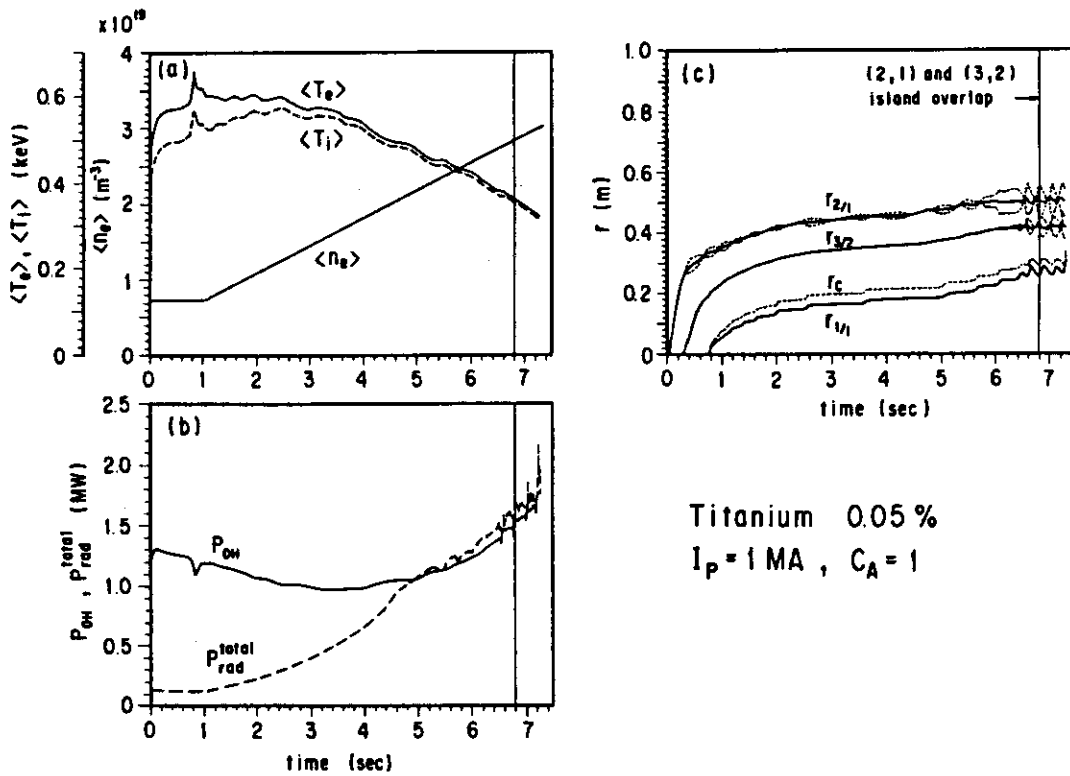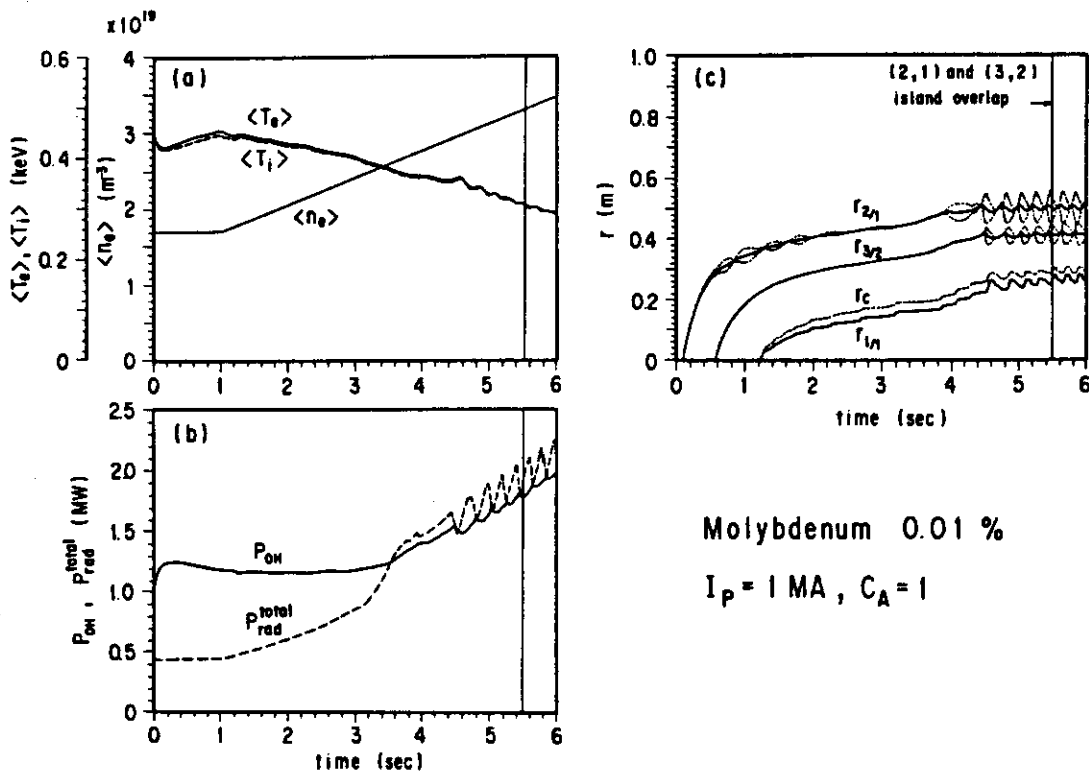

Fig. 18   Time evolution of plasma parameters in I_p=1 MA plasma with 0.05 % titanium.
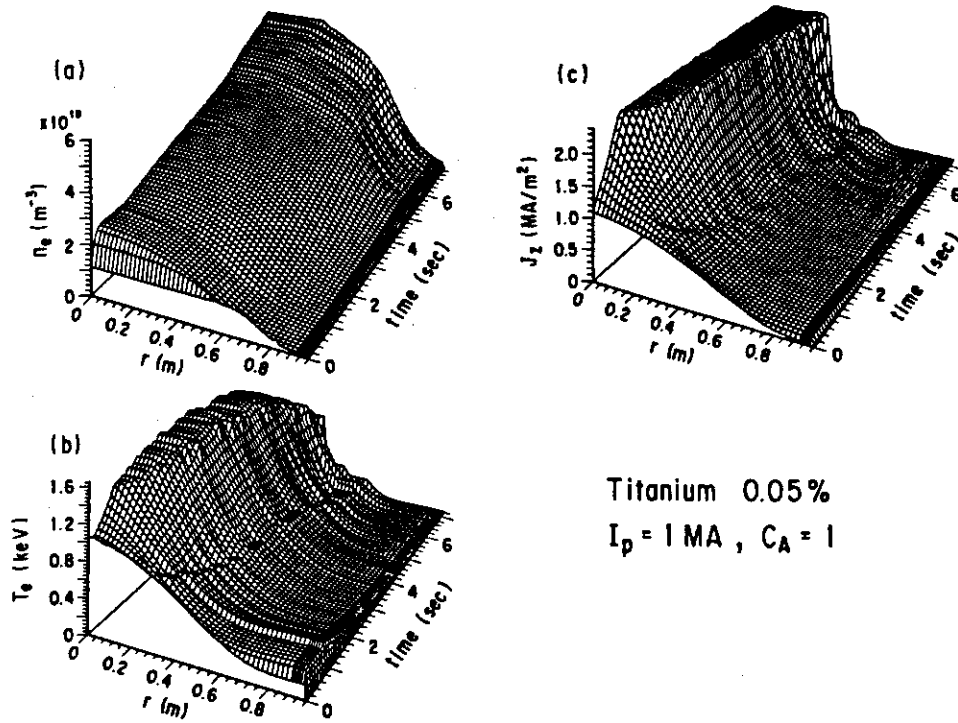
*Fig. 19   Time evolution of n_e, T_e and J_z profiles in $I_p=1$ MA plasma with 0.05 % titanium.*

Fig. 20   Profiles of n_e, T_e, T_i and P_{rad} at $\langle n_e \rangle = 2.18 \times 10^{19}$ m^{-3} ($t=5.0$ sec), $\langle n_e \rangle = 2.78 \times 10^{19}$ m^{-3} ($t=6.7$ sec) and $\langle n_e \rangle = 2.84 \times 10^{19}$ m^{-3} ($t=6.8$ sec) in $I_p=1$ MA plasma with 0.05 % titanium.
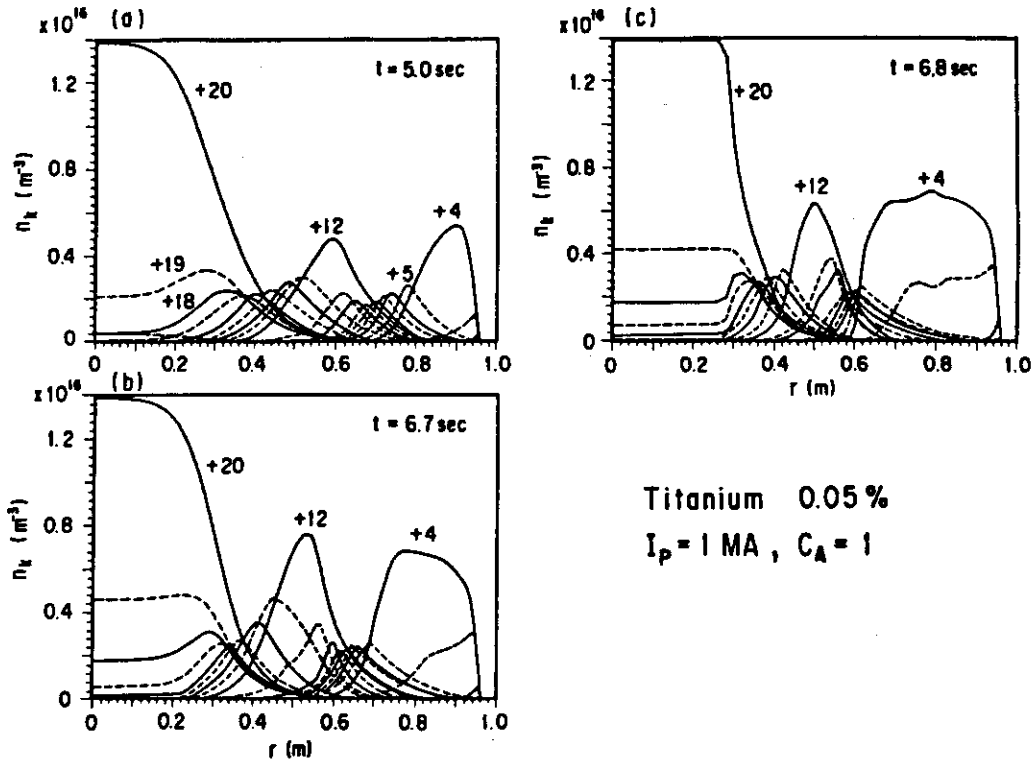
Fig. 21 Profiles of titanium density n_k (k=1, 2, ···, 22) at t=5.0, 6.7 and 6.8 sec in I_p = 1 MA plasma with 0.05 % titanium.

Fig. 22 Time evolution of plasma parameters in I_p=2 MA plasma with 0.05 % titanium.

Titanium 0.05%

$I_P = 2\,MA$, $C_A = 1$
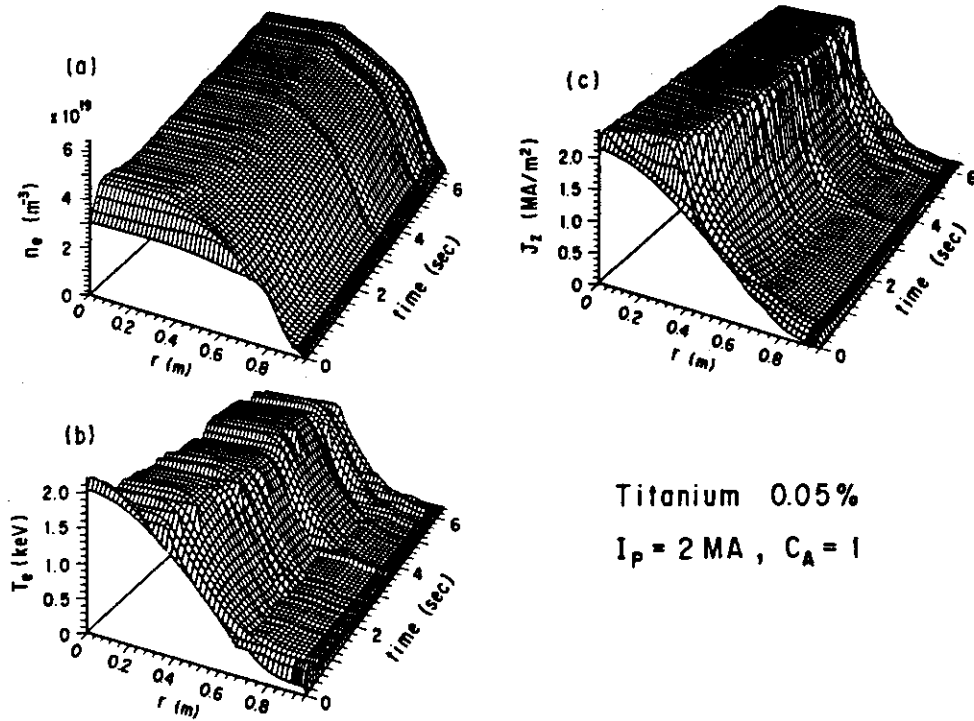
Fig. 23   Time evolution of n_e, T_e and J_z profiles in $I_p=2$ MA plasma with 0.05 % titanium.

Titanium 0.05%

$I_P = 2\,MA$, $C_A = 1$
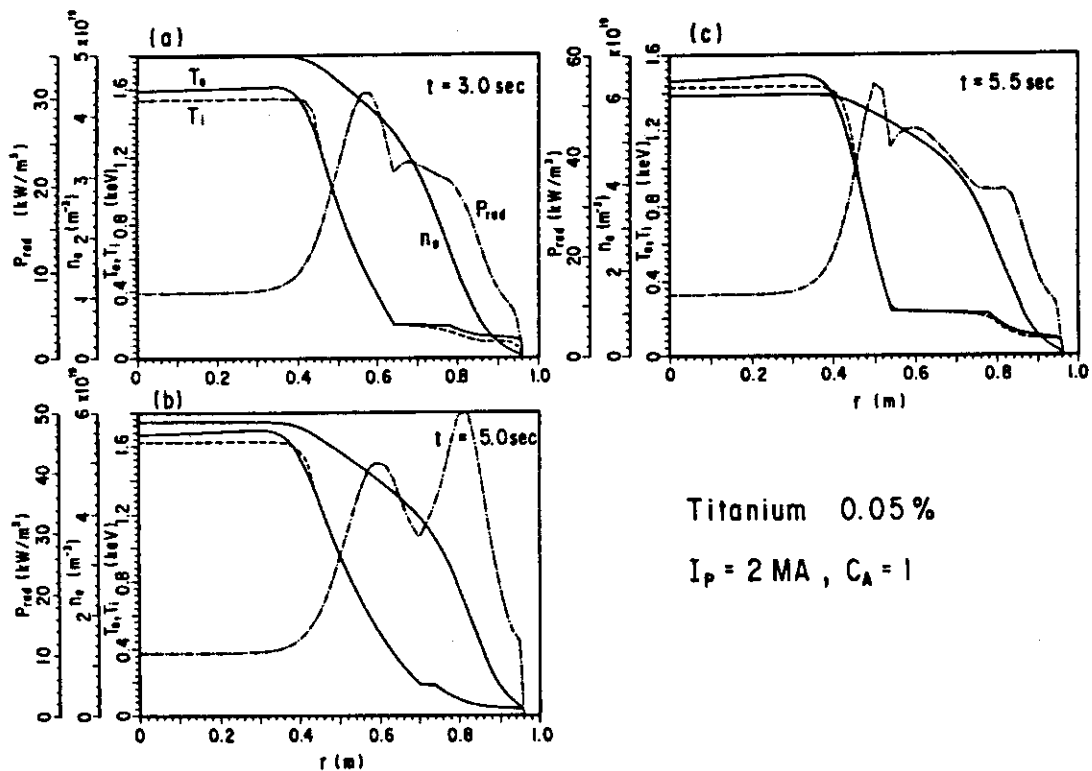
Fig. 24   Profiles of n_e, T_e, T_i and P_{rad} at $\langle n_e \rangle = 2.89 \times 10^{19}$ m^{-3} (t=3.0 sec), $\langle n_e \rangle = 3.63 \times 10^{19}$ m^{-3} (t=5.0 sec) and $\langle n_e \rangle = 3.79 \times 10^{19}$ m^{-3} (t=5.5 sec) in $I_p=2$ MA plasma with 0.05 % titanium.
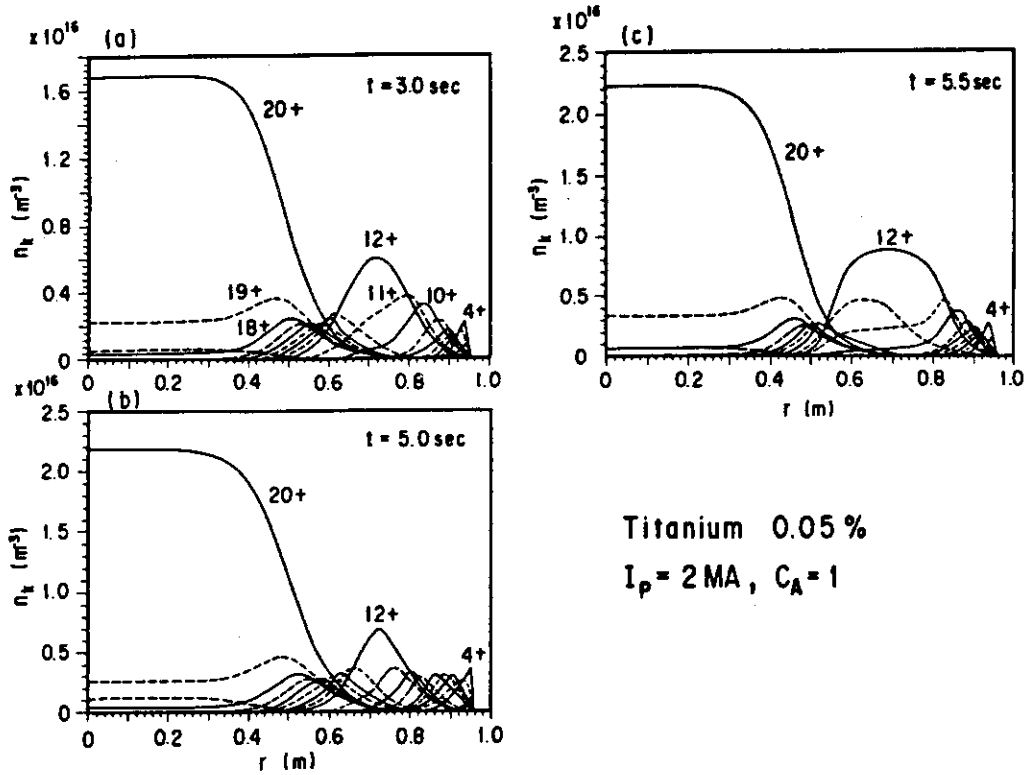
Fig. 25   Profiles of titanium density n_k (k=1, 2, ···, 22) at t=3.0, 5.0 and 5.5 sec in I_p=2 MA plasma with 0.05 % titanium.

Fig. 26   Time evolution of plasma parameters in I_p=1 MA plasma with 0.01 % molybdenum.
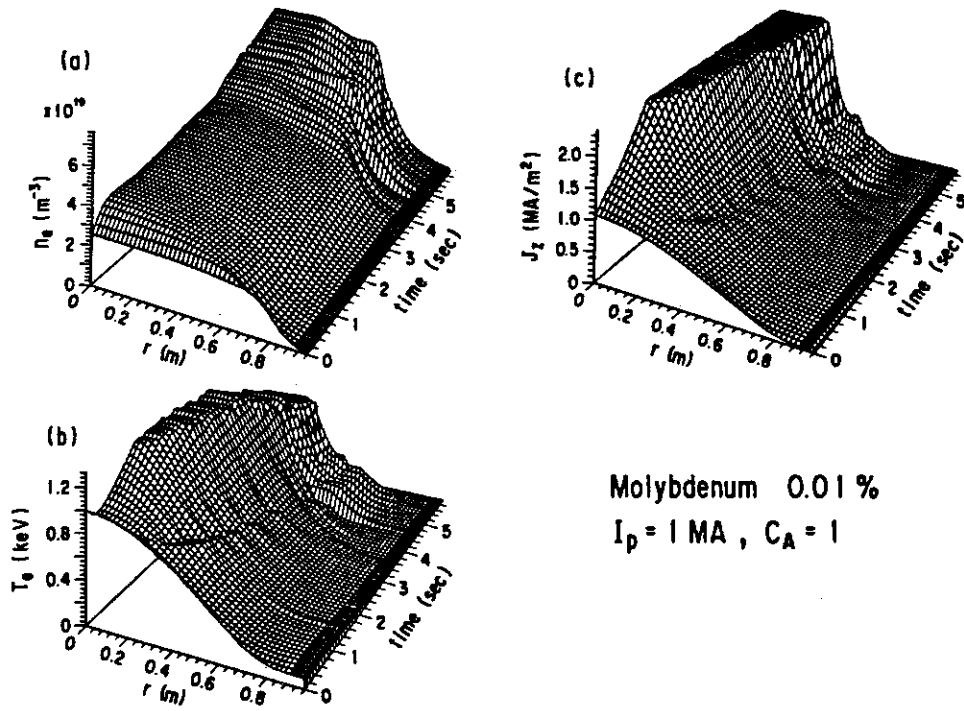
*Fig. 27 Time evolution of n_e, T_e and J_z profiles in $I_p=1$ MA plasma with 0.01 % molybdenum.*
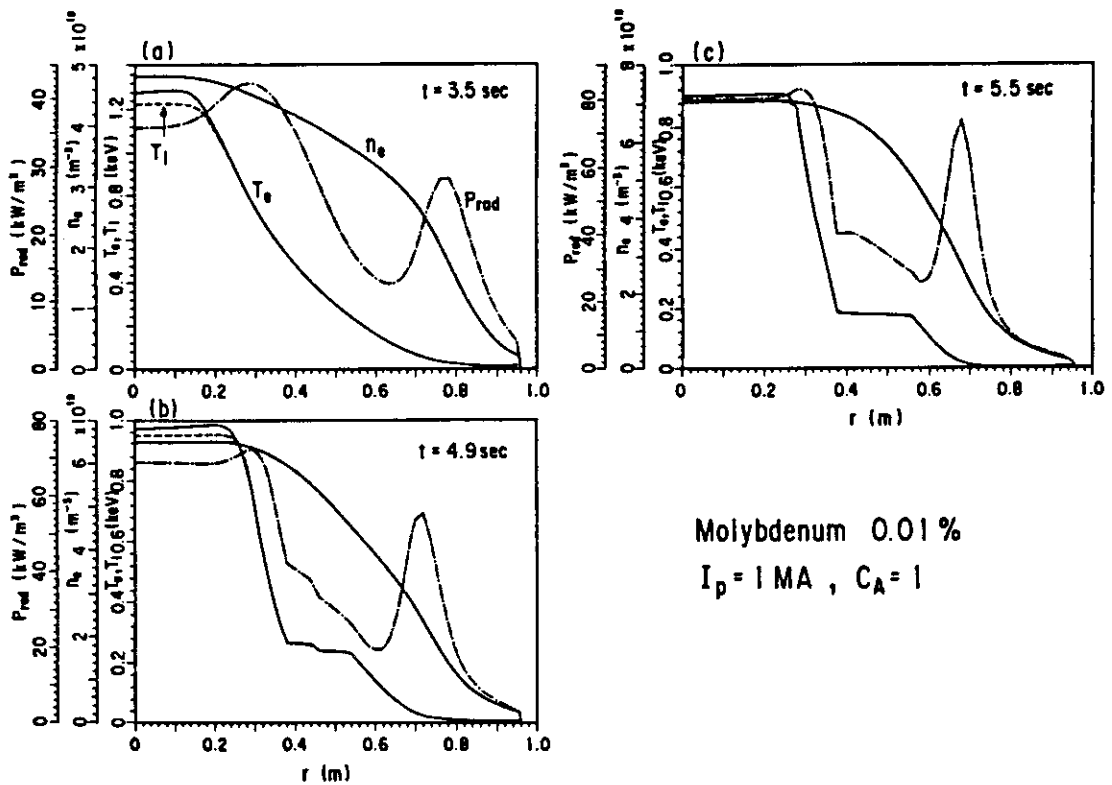
Fig. 28 Profiles of n_e, T_e, T_i and P_{rad} at $\langle n_e \rangle = 2.60 \times 10^{19}$ m^{-3} (t=3.5 sec), $\langle n_e \rangle = 3.10 \times 10^{19}$ m^{-3} (t=4.9 sec) and $\langle n_e \rangle = 3.31 \times 10^{19}$ m^{-3} (t=5.5 sec) in $I_p=1$ MA plasma with 0.01 % molybdenum.
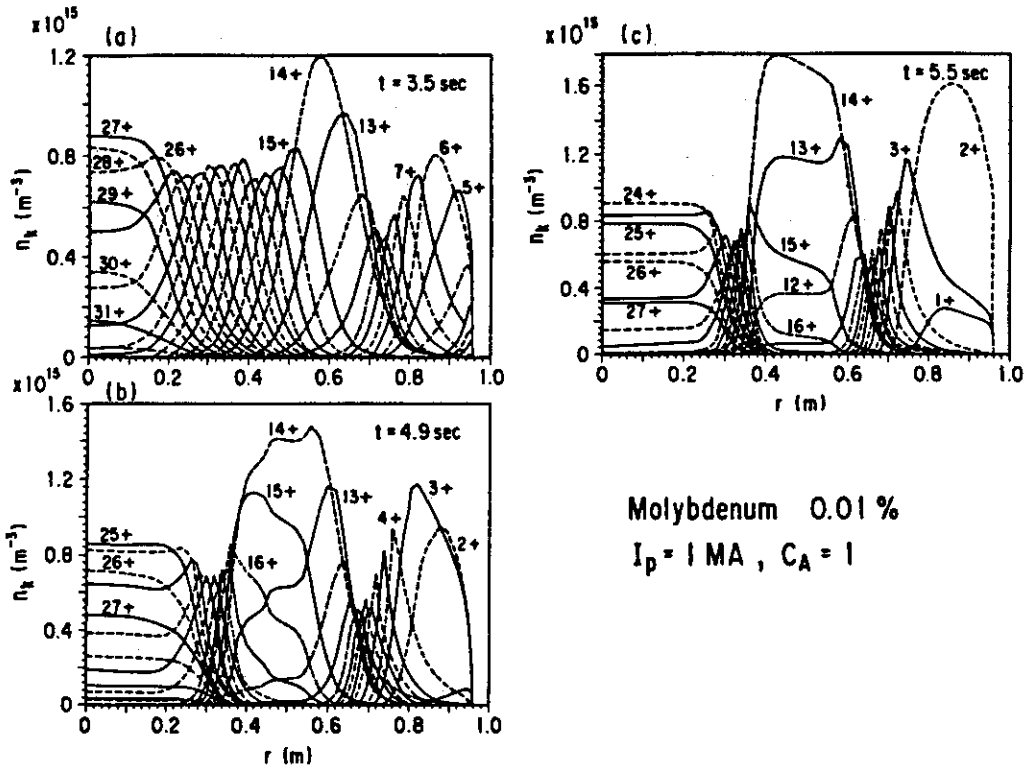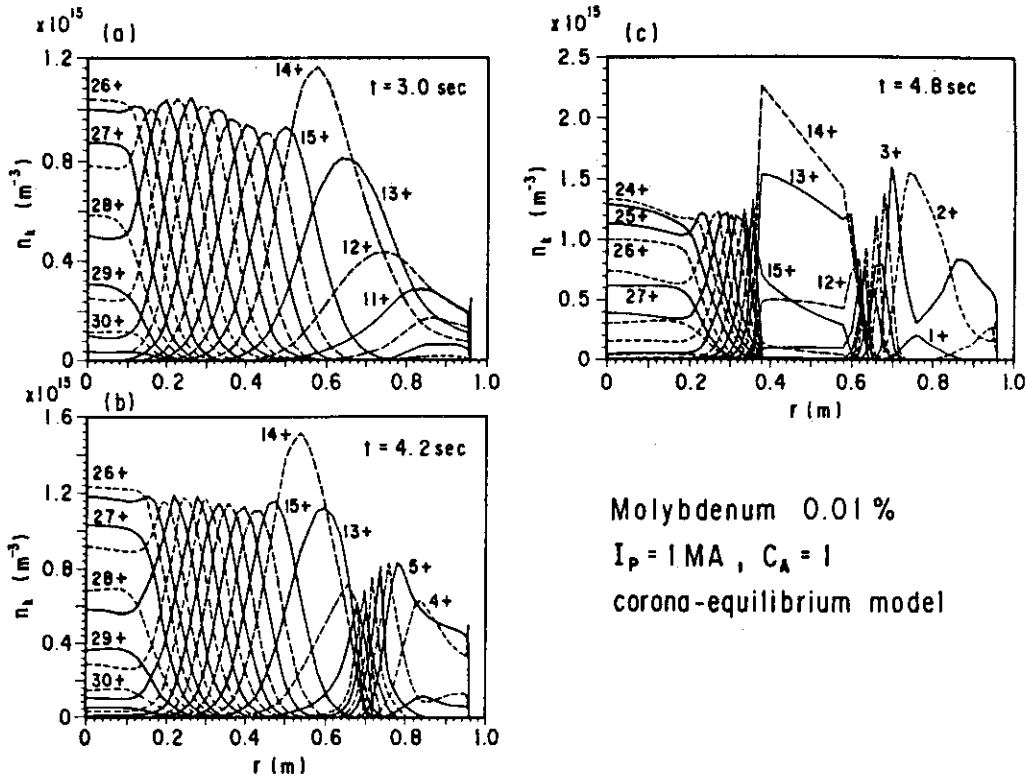
Fig. 29   Profiles of molybdenum density n_k (k=1, 2, $\cdots$, 42) at t=3.5, 4.9 and 5.5 sec in I_p=1 MA plasma with 0.01 % molybdenum.
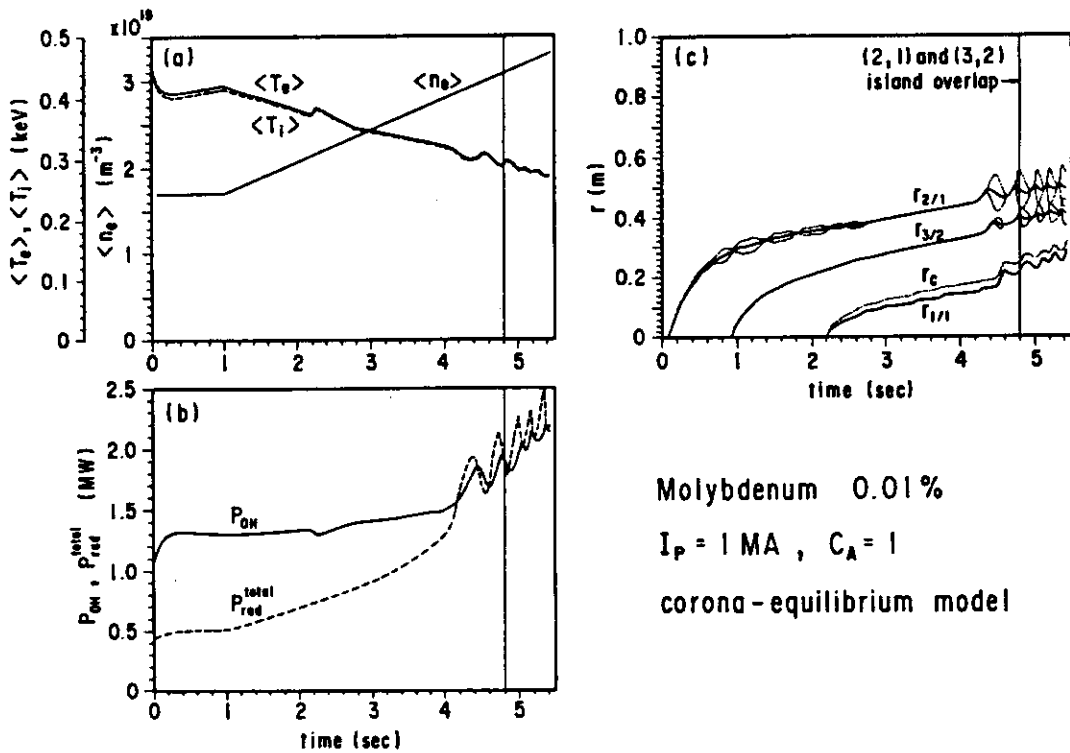
Fig. 30   Time evolution of plasma parameters in I_p=1 MA plasma with 0.01 % molybdenum. The corona-equilibrium model is assumed.
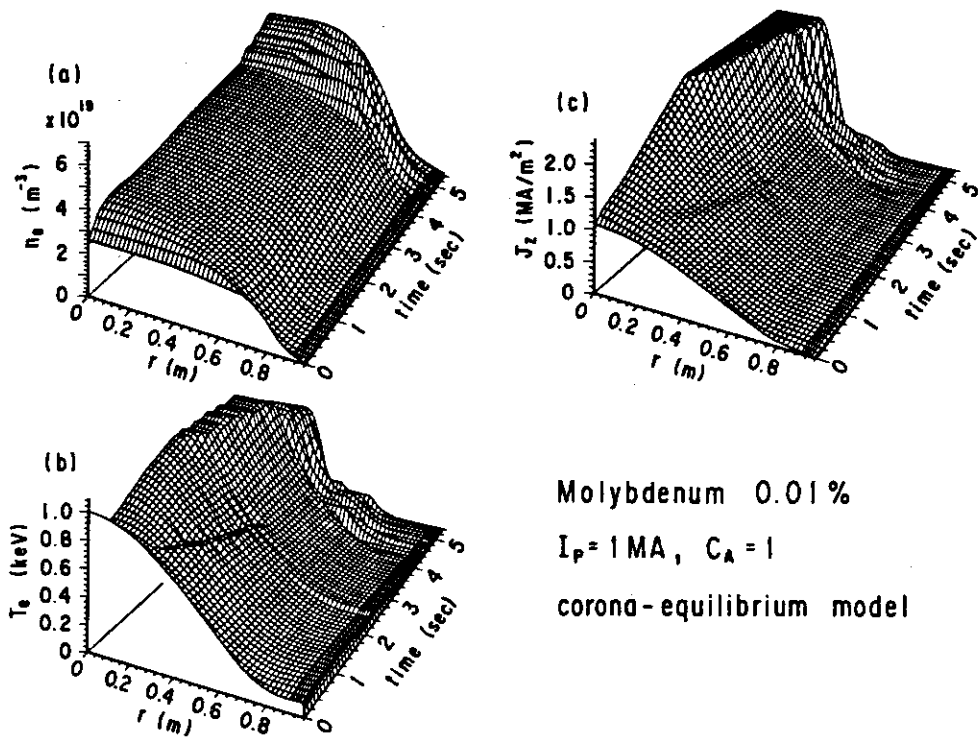
Fig. 31   Time evolution of n_e, T_e and J_z profiles in $I_p=1$ MA plasma with 0.01 % molybdenum. The corona-equilibrium model is assumed.
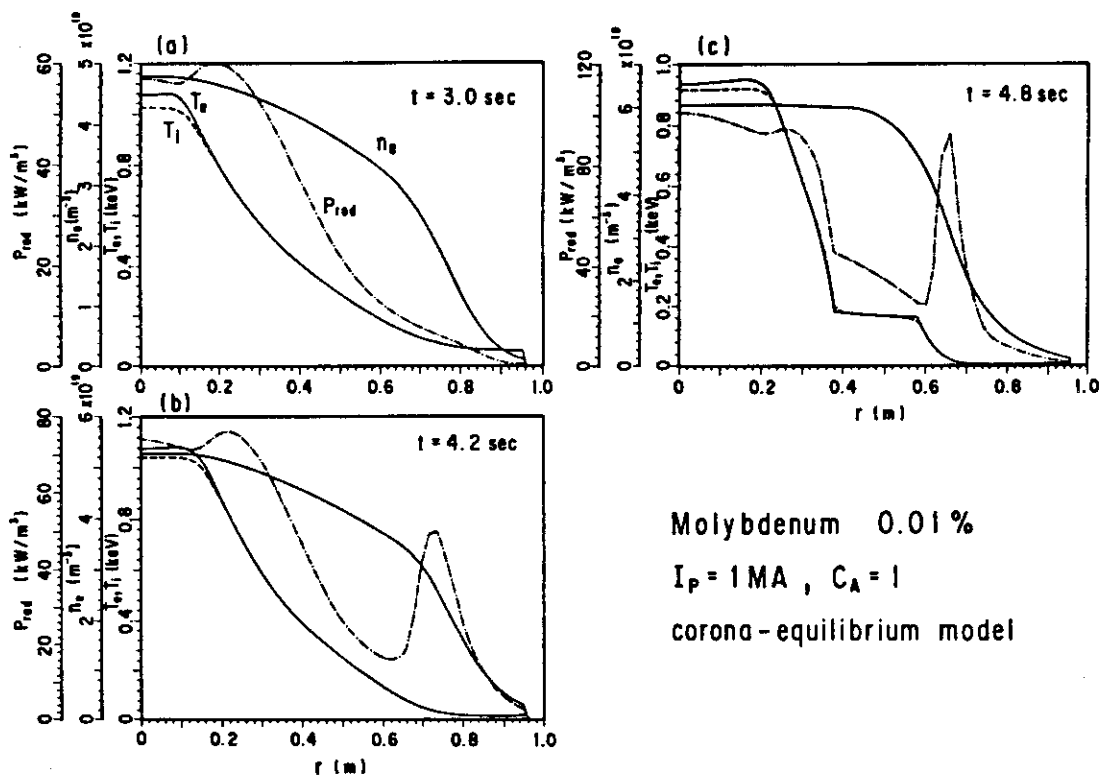
Fig. 32   Profiles of n_e, T_e, T_i and P_{rad} at $\langle n_e \rangle = 2.43 \times 10^{19}$ m^{-3} $(t=3.0$ sec$)$, $\langle n_e \rangle = 2.87 \times 10^{19}$ m^{-3} $(t=4.2$ sec$)$ and $\langle n_e \rangle = 3.08 \times 10^{19}$ m^{-3} $(t=4.8$ sec$)$ in $I_p=1$ MA plasma with 0.01 % molybdenum. The corona-equilibrium model is assumed.

Fig. 33 Profiles of molybdenum density n_k (k=1, 2, $\cdots$, 42) at t=3.0, 4.2 and 4.8 sec in $I_p=1$ MA plasma with 0.01 % molybdenum. The corona-equilibrium model is assumed.
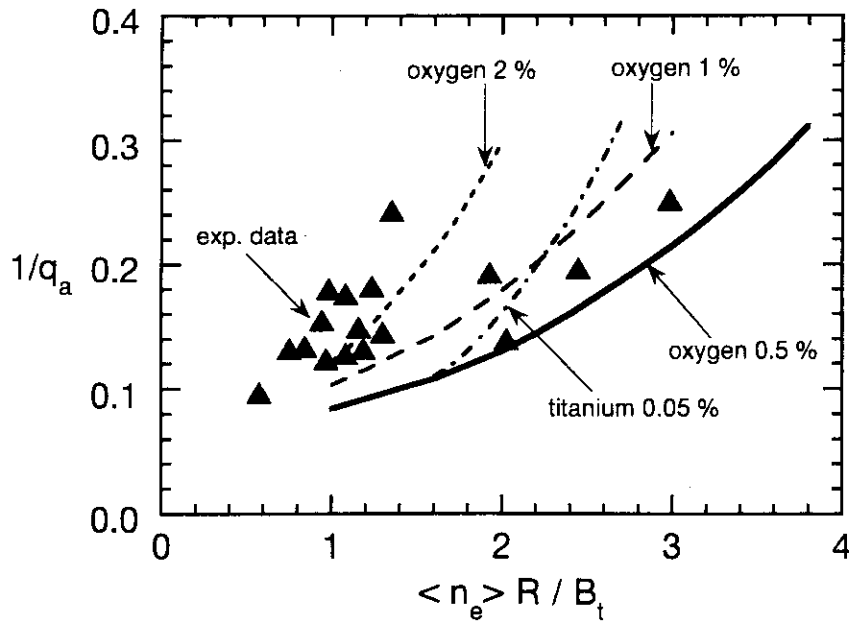
Fig. 34 Hugill diagram by numerical results for various impurity contents in ohmically heated plasmas with $C_A=1$. Experimental data are shown by the closed symbols.
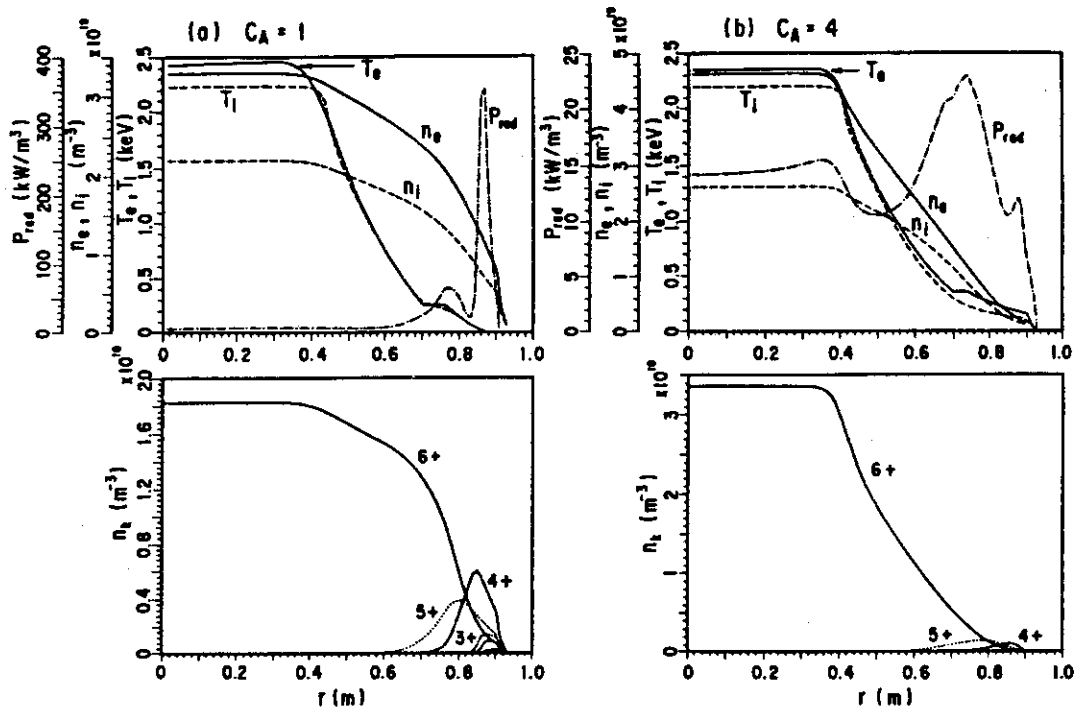
Fig. 35. Comparison of plasma parameter profiles at $\langle n_e \rangle \sim 2.2 \times 10^{19}$ m^{-3} in $I_p = 2$ MA plasma with 6 % carbon in case of $C_A = 1$ and 4.
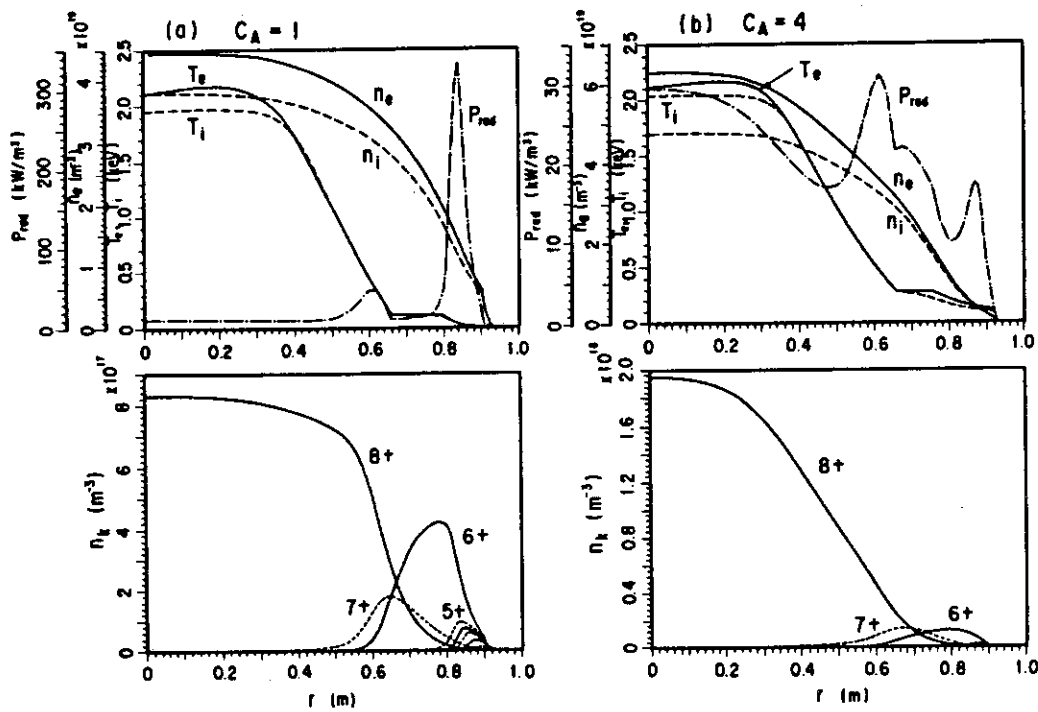
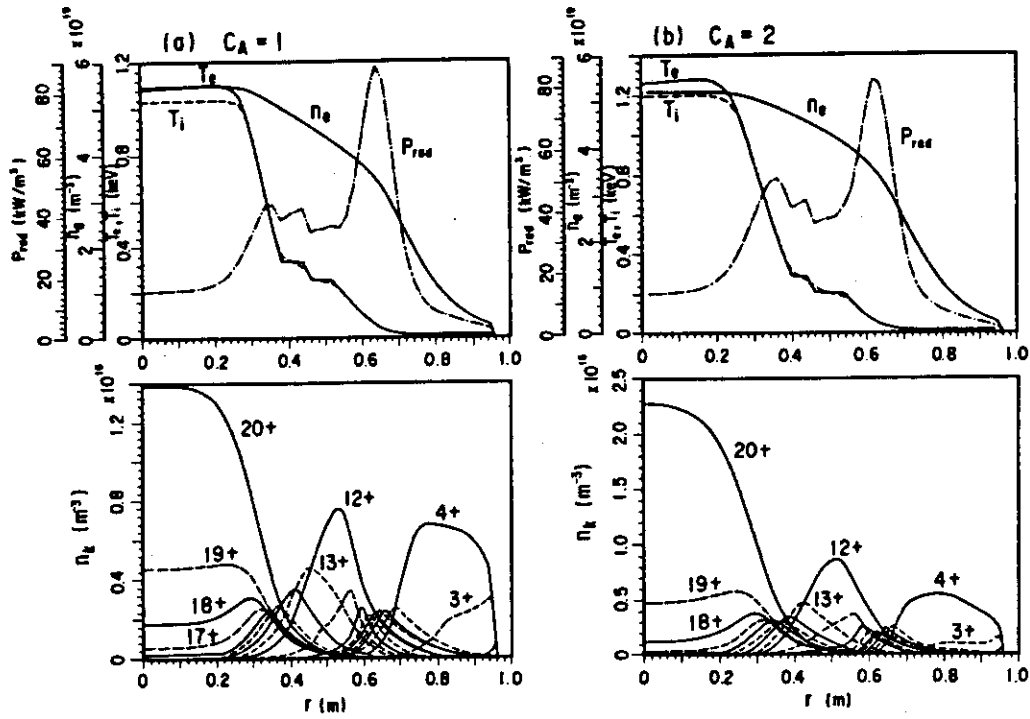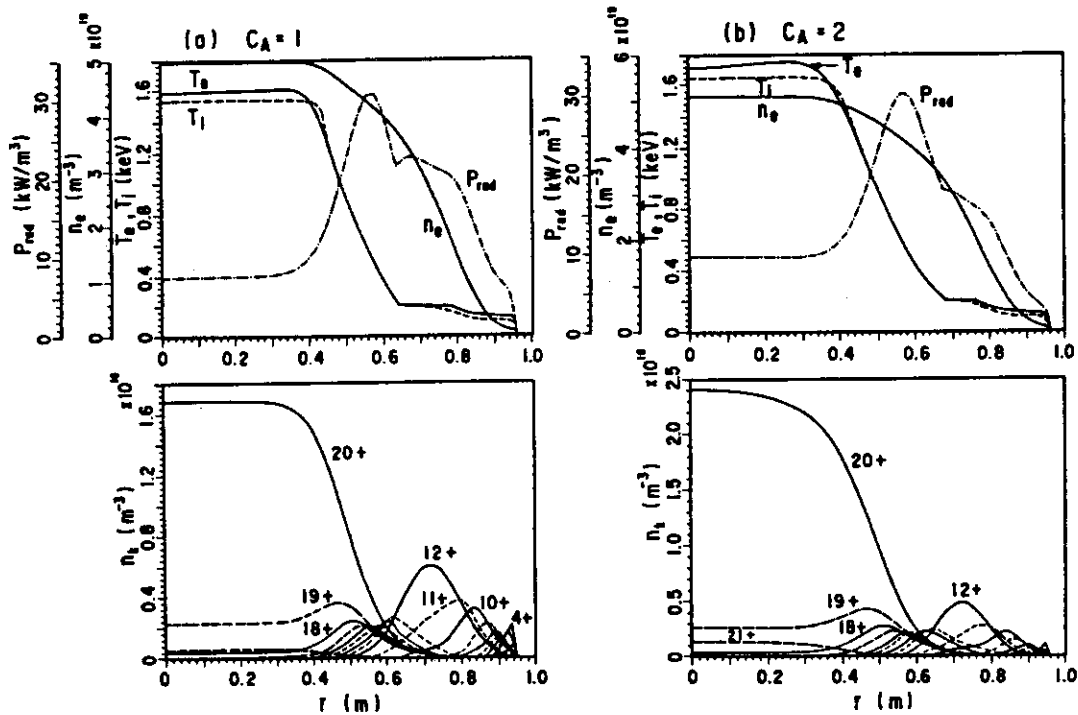Fig. 36 Comparison of plasma parameter profiles at $\langle n_e \rangle \sim 3.0 \times 10^{19}$ m^{-3} in $I_p = 2$ MA plasma with 2 % oxygen in case of $C_A = 1$ and 4.

Fig. 37 *Comparison of plasma parameter profiles at* $\langle n_e \rangle \sim 2.7 \times 10^{19}$ m^{-3} *in* $I_p = 1$ *MA plasma with* 0.05 % *titanium in case of* $C_A = 1$ *and* 2 .

Fig. 38 *Comparison of plasma parameter profiles at* $\langle n_e \rangle \sim 2.9 \times 10^{19}$ m^{-3} *in* $I_p = 2$ *MA plasma with* 0.05 % *titanium in case of* $C_A = 1$ *and* 2 .
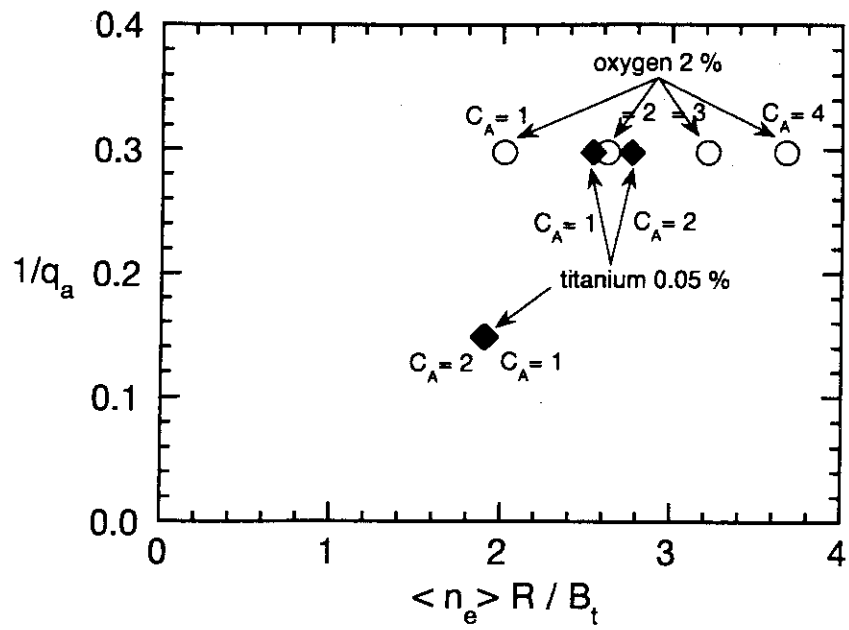
Fig. 39   Hugill diagram by numerical results in ohmically heated plasmas with different C_A value.